Commun Nonlinear Sci Numer Simulat 152 (2026) 109220

Contents lists available at ScienceDirect

Communications in Nonlinear Science and Numerical Simulation

journal homepage: www.elsevier.com/locate/cnsns

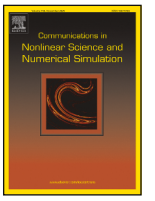

Semi-analytic construction of global transfers between quasi-periodic orbits in the spatial R3BP

Amadeu Delshams [a], Marian Gidea [b], Pablo Roldan [c,*]

[a] Laboratory of Geometry and Dynamical Systems and IMTech, UPC, Barcelona, Spain
[b] Department of Mathematical Sciences, Yeshiva University, New York, NY, 10016, USA
[c] Departament de Matemàtiques, Universitat Politècnica de Catalunya (UPC), Barcelona, 08028, Spain

ARTICLE INFO

Keywords:
Three-body problem
Transfer orbit
Quasi-periodic orbit
Scattering map
Arnold diffusion

ABSTRACT

Consider the spatial restricted three-body problem, as a model for the motion of a spacecraft relative to the Sun-Earth system. We focus on the dynamics near the equilibrium point L_1, located between the Sun and the Earth. We show that we can transfer the spacecraft from a quasi-periodic orbit that is nearly planar relative to the ecliptic to a quasi-periodic orbit that has large vertical amplitude, at zero energy cost. (In fact, the final orbit has the maximum vertical amplitude that can be obtained through the particular mechanism that we consider. Moreover, the transfer can be made through any prescribed sequence of quasi-periodic orbits in between).

Our transfer mechanism is based on selecting trajectories homoclinic to a normally hyperbolic invariant manifold (NHIM) near L_1, and then gluing them together. We present a theoretical result establishing the existence of such transfer orbits, and we verify numerically its applicability to our model. We provide several explicit constructions of such transfers, and also develop an algorithm to design trajectories that achieve the *shortest transfer time* for this particular mechanism.

The change in the vertical amplitude along a homoclinic trajectory can be described via the scattering map. We develop a new tool, the 'Standard Scattering Map' (SSM), which is a series representation of the exact scattering map. We use the SSM to obtain a complete description of the dynamics along homoclinic trajectories. The SSM can be used in many other situations, from Arnold diffusion problems to transport phenomena in applications.

1. Introduction

In this paper, we consider the spatial circular restricted three-body problem (RTBP for short), as a model for the motion of spacecraft relative to the Sun-Earth system. We focus on the dynamics near the equilibrium point L_1 located between the Sun and the Earth. We show that we can transfer the spacecraft, at zero energy cost, from a quasi-periodic orbit that is nearly planar relative to the ecliptic to a quasi-periodic orbit of large vertical amplitude. Moreover, we provide several explicit constructions of such trajectories, and also develop an algorithm to design trajectories that achieve the shortest transfer time. Our algorithm is flexible and can be applied to other systems besides Sun-Earth.

For illustration, Fig. 1 shows the initial and final segments (in blue and green, respectively) of the fastest transfer trajectory between one quasi-periodic orbit with small vertical amplitude, and another with large vertical amplitude.

The model that we consider is a 3-degrees of freedom Hamiltonian system. We construct trajectories that follow closely geometric structures that organize the dynamics. The main geometric object near L_1 is a 4-dimensional center manifold on which the dynamics

* Corresponding author.
E-mail address: Pablo.Roldan@upc.edu (P. Roldan).

https://doi.org/10.1016/j.cnsns.2025.109220

Available online 19 August 2025

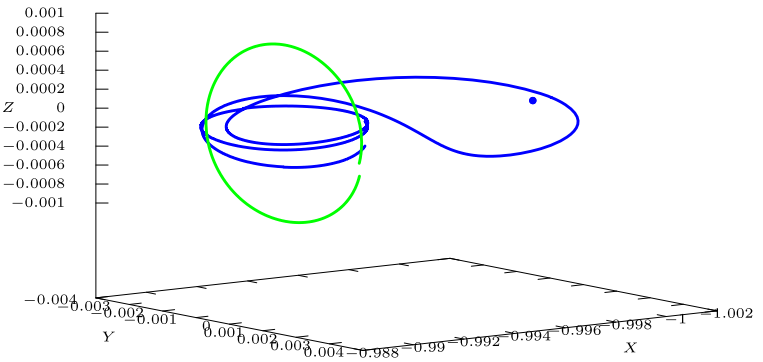

Fig. 1. Initial segment (blue) and final segment (green) of the fastest transfer trajectory between a quasi-periodic orbit with small vertical amplitude (small Z-oscillation), and another with large vertical amplitude (Z-oscillation of amplitude 0.001, roughly 150,000 km). The complete trajectory (not shown here) is very complicated, and goes through many homoclinic jumps. This trajectory is computed in Section 12.2. (See also Figs. 20 and 21).

is nearly integrable. More precisely, in a neighborhood of L_1 the Hamiltonian can be approximated by a high-order Birkhoff normal form, which is an integrable Hamiltonian. In terms of the Birkhoff normal form, the center manifold can be parametrized by a system of symplectic coordinates consisting of two action variables (J_p, J_v) and two angle variables (ϕ_p, ϕ_v). The action J_p describes the horizontal amplitude (relative to the ecliptic) of a quasiperiodic orbit, and J_v describes its vertical amplitude. Restricting to an energy level close to that of L_1 amounts to fixing the action variable J_p. This yields a 3-dimensional sphere which is foliated by 2-dimensional tori, where each torus is uniquely determined by a fixed value of the remaining action variable J_v. A change in J_v corresponds to a change in the vertical amplitude of a quasi-periodic orbit. Since the tori are invariant, by using only the 'inner flow' restricted to the 3-dimensional sphere, the vertical amplitude of orbits remains constant. However, the tori do not separate the energy manifold, so there may exist trajectories that move from one torus to another, thus changing the vertical amplitude. In order to obtain such trajectories, we need to use the 'outer dynamics', described below.

The 3-dimensional sphere is a normally hyperbolic invariant manifold (NHIM), and has stable and unstable manifolds which go around the Earth and intersect transversally along trajectories homoclinic to the NHIM. By carefully selecting consecutive homoclinic trajectories, we show that it is possible to achieve large changes in the vertical amplitude of orbits. Proving the existence of such trajectories is related to *Arnold diffusion problem* (see the discussion later).

The tool that allows us to systematically select suitable homoclinics at each step is the *scattering map*. This is a map defined on the NHIM, which relates the past asymptotic of a homoclinic point to its future asymptotic. The scattering map was introduced in Delshams et al. [1,2,3] in the study of Arnold diffusion. When restricted to a suitable 2-dimensional Poincaré section, the scattering map turns out to be symplectic [4,5]. An additional advantage that we exploit in our model is that we obtain two scattering maps, which give us more options in the selection of suitable homoclinics.

We provide a theoretical result (Theorem 1) that gives sufficient conditions on a inner dynamics and two scattering maps defined on an annulus inside a NHIM (described in action-angle variables), to ensure the existence of true trajectories that start near the lower boundary of the annulus and end near its upper boundary.

In our model, the action variable corresponds to the vertical amplitude J_v and the annulus to some range of $J_v \in [J_1, J_2]$. Provided that the assumptions of Theorem 1 are verified, the orbits of the Iterated Functions System (IFS) formed by the two scattering maps and the inner map that achieve the prescribed gain in the vertical amplitude yield true trajectories that achieve the same gain (up to a small error). To distinguish the orbits of the IFS from true trajectories of the system, we will refer to the former as *pseudo-orbits*.

Before going into more details, we now outline the methodology that we will use. The trajectories designed to change the vertical amplitude J_v are guided by homoclinic orbits that depart and land, asymptotically, at points in the NHIM, depending on the scattering (outer) map used. The vertical amplitude at landing can be higher or lower than the vertical amplitude at departure. The inner dynamics of the NHIM allow us to travel between points with the same vertical amplitude to change, if necessary, the departure points. With a simple simulation of these 3 dynamics—the 2 scattering maps and the inner map—we obtain pseudo-orbits with the desired vertical amplitude gain.

We note that the problem that we consider is not perturbative. Until now, the only available methods for computing the scattering map in such a setting have been numerical [6,7]. However, purely numerical approaches are computationally intensive and offer little insight into the geometric structures determined by the scattering map.

The highlight of this paper is that we provide an analytical approximation of the scattering map for the spatial circular RTBP. We describe the scattering map via a generating function depending on old and new variables. Then we approximate the generating function using a Fourier-Polynomial interpolation. As it turns out, the numerical computation of the scattering map at a few points can be used to compute the coefficients of the Fourier-Polynomial interpolation, up to some suitable order, and thus to obtain an analytical formula for the generating function, up to some small error. The outcome of this approximation is referred to as the *Standard Scattering Map* (SSM). It is given explicitly as a perturbation of an integrable twist map. As such, the phase space of the scattering map is organized by KAM tori, elliptic islands, hyperbolic periodic orbits and their stable and unstable manifolds, and resonant

zones. See Fig. 14. The rich geometric structure unveiled by the analytical approximation of the scattering map was not available through previous approaches. Similar computations of the generating function of the scattering map and of its phase space were obtained purely analytically in *uncoupled* pendulum-rotor systems subject to small perturbations of a special type [8,9]. However, as the unperturbed pendulum-rotor systems considered in those papers are uncoupled, the phase shift phenomenon [10] does not take place, and the unperturbed scattering maps are just the identity. In particular, they are not twist maps, which makes the dynamics different from those considered in this paper.

The main application of the Standard Scattering Map is that it offers an explicit method to find pseudo-orbits, that is, orbits of the iterated function system consisting of scattering maps and the inner map (induced by the inner flow on the Poincaré section), along which the vertical amplitude J_v grows consistently. The method is versatile, in the sense that one can choose the starting and ending points of such pseudo-orbits. As mentioned earlier, in this paper we compute two scattering maps, and we compare them in terms of the fastest trajectory to achieve the desired change in vertical amplitude.

It is important to note that the orbits of the scattering maps are not equivalent to true trajectories of the system. Rather, we can approximate a segment of a homoclinic trajectory by a concatenation of a finite orbit of the inner dynamics, followed by an application of a scattering map, followed by another finite orbit of the inner dynamics. The map that described this concatenation of orbits is referred to as the *transition map*. The transition map is a map on the NHIM, and each application of the transition map approximates a segment of a homoclinic orbit to the NHIM; see Section 2.4. Since we have constructed two scattering maps, we have two corresponding transition maps. To obtain approximate trajectories that change the orbital vertical amplitude, we consider the iterated function system consisting of the two transition maps and the inner map, and we search for optimal trajectories.

Note the order in which our methodology proceeds. First and foremost, we obtain the Standard Scattering Map, which models the asymptotic homoclinic dynamics in a comprehensive and efficient manner, forming the backbone of all subsequent computations. Second, we use the SSM to validate the hypothesis of Theorem 1 and conclude the existence of diffusion. However, to design pseudo-orbits it is necessary to work with finite-time segments of trajectories. Third, from the SSM we derive the transition map, which approximates *finite-time* homoclinic segments. The transition map is used to design pseudo-orbits, which can finally be refined into true orbits.

To find optimal pseudo-orbits, we leverage the classic Dijkstra algorithm for finding shortest paths in a graph. A surprising finding is that for an optimal orbit of the iterated function system, rather than always selecting a transition map that grows J_v, sometimes we must select a transition map that decreases J_v, in order to arrive to a place where the next application of a transition map yields a large increase in J_v. Another surprising finding is that an optimal pseudo-orbit involves very few applications of the inner map.

More quantitatively, in Section 12 we divide the phase space into a grid of $30 \times 30 = 900$ small cells, and in Section 12.2 we obtain a diffusion pseudo-orbit that uses just 17 iterations of the scattering/transition maps plus intermediate iterations of the inner map. We emphasize that only using the image of 7 tori we can have an approximation of the phase space of the scattering map, good enough to be able to design with several algorithms the appropriate diffusion pseudo-orbits. The use of more invariant tori and of a more refined grid does not present additional technical difficulties, and would not modify in a qualitative way the phase space of the scattering maps represented in Fig. 14, so the optimal paths would not change substantially.

These optimal pseudo-orbits can be refined into true orbits either through theoretical shadowing results or by applying appropriate numerical methods, such as parallel shooting.

Our construction described so far is based on approximating the Hamiltonian near L_1 by a Birkhoff normal form. Since the approximation is quite accurate, the true dynamics associated to the original Hamiltonian follow closely the Birkhoff normal form dynamics. In particular, the trajectories of the true inner dynamics stay close to invariant tori, and the scattering map for the true dynamics is close to the scattering map derived from the normal form approximation. This implies that there exist diffusing trajectories—that change the orbital vertical amplitude by a significant amount—for the original Hamiltonian system.

Our results are related to the Arnold diffusion problem for Hamiltonian systems, claiming that integrable Hamiltonian systems subjected to small perturbations of generic type have 'diffusing orbits' along which the action variable changes by an amount independent of the smallness of the perturbation [11]. Arnold proposed a mechanism of diffusion based on transition chains of tori, which are sequences of invariant tori with consecutive heteroclinic connections between consecutive tori. Arnold conjectured: "I believe that this mechanism of instability is applicable to the general case (for example, to the problem of three bodies)". This conjecture has witnessed significant progress in recent years, including [1–3,12–29]. Some of the progress has been geared towards proving Arnold diffusion in concrete models, under explicit, verifiable conditions on the perturbation. This direction opened up the possibility of implementing Arnold's mechanism of diffusion in applications, such as to Celestial Mechanics. Notably, some papers, including [30–32], succeeded in providing analytical proofs of Arnold diffusion in some models of the three- and four-body problem. These papers rely on perturbative methods, and therefore they need to assume that certain parameters (such as ratios of the masses of the bodies, or ratios of the semi-major axes of the orbits) are very small, in fact much smaller than those observed in solar systems. Another line of arguments combine analytical methods with numerical computation (including computer assisted proofs) to show Arnold diffusion in models with realistic parameters, see, e.g. Capiński et al. [33], Capiński and Gidea [34], Figueras and Haro [35].

Our paper follows this latter approach. In the case of the Sun-Earth system we implement Arnold's mechanism of transition chains of tori via analytical tools and numerical methods, obtaining orbits that follow the transition chain and change their vertical amplitude. The system that we consider is *a priori chaotic*, that is, it contains a hyperbolic basic set (see, e.g., Gelfreich and Turaev [27]). Since the system is non-perturbative, we do not obtain a change that is independent of some small parameter. However, we argue that the change is as large as possible for the geometric mechanism at play. Specifically, we obtain a change in the action that spans approximately 70 % of the region where primary homoclinic orbits exist. (See Section 4.5).

The construction in this paper can be potentially adapted to astrodynamics applications. Sometimes, a satellite (which typically carries little fuel) ends up on a wrong orbit, and one tries to correct the orbit by exploiting the gravity of Earth, Sun, Moon as much as possible, and firing the satellites' thrusters as little as possible; see, e.g., Belbruno [36]. While our methodology to change the vertical amplitude of a satellite orbit may be too slow from a practical point of view, by combining zero-cost geometric routes with small thrusts, one may be able to design useful trajectories; see, e.g., Gómez et al. [37].

This paper does not focus on trajectory optimization. Nevertheless, in our setting, we can estimate both the duration (32 years) and the total required thrust (271 m/s) for the pseudo-orbit that exhibits the fastest growth in vertical amplitude. See Section 12.2 and Remark 19.

Moreover, our methodology can be applied to build transfers involving two or more NHIMs connected by heteroclinic orbits, e.g., the NHIM around L_1 and that around L_2 [10,38].

2. Setup

2.1. The spatial circular RTBP

We consider the spatial circular RTBP as a model for the motion of an infinitesimal body (e.g. satellite) under the gravitational influence of two massive bodies, referred to as primaries (e.g. Sun and the Earth). We describe the problem in normalized units, relative to a co-rotating frame XYZ, such that the larger primary of mass $1-\mu=\mu_1$ is located at $P_1=(\mu,0,0)$, the smaller primary of mass μ is located at $P_2=(\mu-1,0,0)$, and the vertical component of the motion of the infinitesimal body is given by the Z-coordinate (see Fig. 2).

In the case of the Sun-Earth system $\mu=3.040423398444176\times10^{-6}$.

The motion of the infinitesimal body relative to these coordinates is given by the autonomous system of equations:

$$\begin{aligned}\ddot{X}-2\dot{Y}&=\Omega_X,\\ \ddot{Y}+2\dot{X}&=\Omega_Y,\\ \ddot{Z}&=\Omega_Z,\end{aligned}\tag{1}$$

where the effective potential Ω is given by

$$\Omega=\frac{1}{2}(X^2+Y^2)+\frac{1-\mu}{r_1}+\frac{\mu}{r_2},$$

with r_1, r_2 representing the distances from the secondary to the larger and the smaller primary, respectively:

$$\begin{aligned}r_1&=\left((X-\mu)^2+Y^2+Z^2\right)^{1/2},\\ r_2&=\left((X-\mu+1)^2+Y^2+Z^2\right)^{1/2}.\end{aligned}$$

The phase space is 6-dimensional.

The system has an integral of motion (referred to as the Jacobi integral) given by:

$$C=2\Omega-(\dot{X}^2+\dot{Y}^2+\dot{Z}^2).$$

Equivalently, the Eq. (1) can be described as a 3-degree-of-freedom, autonomous Hamiltonian system given by the Hamiltonian function:

$$H=\frac{1}{2}\left(P_X^2+P_Y^2+P_Z^2\right)+YP_X-XP_Y-\frac{1-\mu}{r_1}-\frac{\mu}{r_2},\tag{2}$$

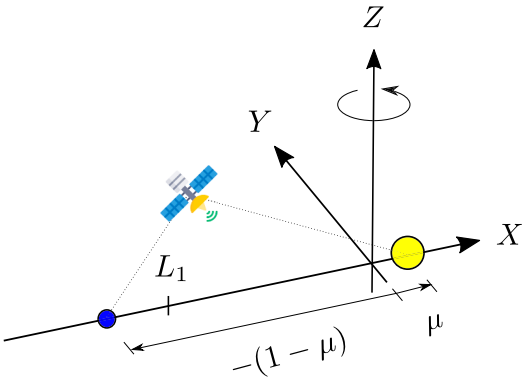

Fig. 2. Schematic location of the Sun (in yellow), the Earth (in blue), and the equilibrium point L_1.

where X, Y, Z are the generalized coordinates, $P_X = \dot{X} - Y$, $P_Y = \dot{Y} + X$, $P_Z = \dot{Z}$ are the generalized momenta, and the symplectic form is:

$$dP_X \wedge dX + dP_Y \wedge dY + dP_Z \wedge dZ.$$

We denote by Φ_H the flow of (2).

The Hamiltonian function and the Jacobi integral are equivalent integrals of motion, since

$$H = -C/2.$$

As the Hamiltonian (and, equivalently, the Jacobi integral) is preserved along the solutions of the system, each trajectory lies on a 5-dimensional energy manifold M_c corresponding to some energy level $h = -c/2$, that is,

$$M_c = \{H(P_X, P_Y, P_Z, X, Y, Z) = -c/2\}.$$

In this paper we focus on the dynamics around the equilibrium point L_1, which is located between the primaries, and is of Saddle × Center × Center – linear stability type (see Fig. 2). Let us denote by

$$\pm\lambda, \pm i\nu_p, \pm i\nu_v, \text{ with } \lambda, \nu_p, \nu_v \text{ real and positive,}$$

the eigenvalues of the linearized system near L_1. The quantities $\lambda, -\lambda$ represent the exponential expansion and contraction hyperbolic rates, while ν_p, ν_v represent the frequencies of the planar and vertical components of the motion, respectively. In the case of the Sun-Earth system, $\lambda = 2.5326591740529678$, $\nu_p = 2.0864535642231075$ and $\nu_v = 2.0152106629966386$.

By the Center Manifold Theorem (see e.g., Jorba and Masdemont [39]), there exists a 4-dimen-sional invariant center manifold $\Lambda = W^c(L_1)$ that is tangent at L_1 to the generalized eigenspace corresponding to $\pm i\nu_p, \pm i\nu_v$. The manifold Λ is a normally hyperbolic invariant manifold (NHIM) for the flow Φ_H. If we fix the energy level (or, equivalently the Jacobi constant), the restriction of the center manifold $W^c(L_1)$ to the energy level $\{H = -c/2\}$ is a 3-dimensional sphere

$$\Lambda_c = \Lambda \cap M_c,$$

which is a NHIM for the flow Φ_H restricted to the energy manifold M_c.

2.2. Local dynamics around L_1

The Hamiltonian H can be expanded about L_1, via a symplectic coordinate change

$$(P_X, P_Y, P_Z, X, Y, Z) \mapsto (y_h, J_p, J_v, x_h, \phi_p, \phi_v),$$

as a Birkhoff normal form

$$\mathcal{H}^{(N)} = H_2 + \mathcal{Z}^{(N)} + \mathcal{R}^{(N)},$$

where H_2 denotes the quadratic part of H expressed in terms of the new variables, $\mathcal{Z}^{(N)}$ is a polynomial of degree N that Poisson-commutes with H_2, and the remainder $\mathcal{R}^{(N)}$ is small in a neighborhood of L_1 (more precisely, of the order of the $(N+1)$th power of the distance to L_1). The coordinates x_h, y_h represent the hyperbolic directions of motion. The *action variables* (J_p, ϕ_p) correspond to the *planar* component of the motion, while the *angle variables* (J_v, ϕ_v) corresponds to the *vertical* component. A useful reference for the derivation of such a Birkhoff normal form is Jorba [40].

In [7], we performed the computation of this normal form for the spatial circular RTBP up to order $N = 16$. We will use this computation in this paper.

The truncated Birkhoff normal form depends only on $x_h y_h$, J_p, J_v,

$$\mathcal{H}^{(N)}_{\text{trunc}} = H_2 + \mathcal{Z}^{(N)} = \lambda x_h y_h + \nu_p J_p + \nu_v J_v + \mathcal{Z}^{(N)}(x_h y_h, J_p, J_v), \tag{3}$$

which are integrals of motion for $\mathcal{H}^{(N)}_{\text{trunc}}$. We denote by Φ_N the flow associated to (3).

The truncated Birkhoff normal form $\mathcal{H}^{(N)}_{\text{trunc}}$ represents an approximation of the original Hamiltonian H, and therefore the invariant objects for $\mathcal{H}^{(N)}_{\text{trunc}}$ give approximations of the corresponding invariant objects of H. Truncating the normal form at order $N = 16$ ensures that the error between the true dynamics in the NHIM and the dynamics induced by the Birkhoff normal form is within machine precision. See Section 4.1. In particular, we consider the center manifold Λ^N for the truncated Birkhoff normal $H^{(N)}_{\text{trunc}}$, which represents an approximation of Λ. In the action-angle coordinates, we have that

$$\Lambda^N = \left\{(y_h, J_p, J_v, x_h, \phi_p, \phi_v) \,|\, y_h = 0, x_h = 0, J_p, J_v \geq 0,\ \phi_p, \phi_v \in \mathbb{T}\right\}, \tag{4}$$

is parameterized by the symplectic action-angle coordinates $(J_p, J_v, \phi_p, \phi_v)$. This has a symplectic structure given by the form

$$dJ_p \wedge d\phi_p + dJ_v \wedge d\phi_v.$$

The planar Lyapunov periodic orbits correspond to $J_v = 0$ and $J_p > 0$, the vertical Lyapunov periodic orbits to $J_p = 0$ and $J_v > 0$, and the libration point L_1 to $J_p = J_v = 0$, so these coordinates are degenerate when some action $J_{p,v} = 0$, as it is usual with polar coordinates.

For a fixed energy $\mathcal{H}^{(N)}_{\text{trunc}} = h = -c/2$, J_p is given as an implicit function of J_v, ϕ_p, ϕ_v, c. The corresponding NHIM for the truncated system is given by

$$\Lambda^N_c = \Lambda^N \cap \left\{ \mathcal{H}^{(N)}_{\text{trunc}} = -c/2 \right\},$$

and is therefore parameterized by the 3 variables (J_v, ϕ_p, ϕ_v).

For each fixed value of the vertical action $J_v = \bar{J}_v$, there is a unique invariant torus for the Birkhoff normal form

$$T^N_{\bar{J}_v} = \Lambda^N_c \cap \{J_v = \bar{J}_v\}$$

which is therefore parameterized by the 2 angles (ϕ_p, ϕ_v). Thus, the NHIM Λ^N_c is foliated by a family of 2-dimensional invariant tori. By comparison, the NHIM Λ_c corresponding to the full Hamiltonian H contains a KAM family of 2-dimensional invariant tori, with gaps between the tori that are exponentially small in the action (see Capiński and Roldán [41] for quantitative estimates). The existence of the NHIM for the full Hamiltonian has been rigorously proven for the planar RTBP in Capiński and Roldán [41].

Each of the objects Λ^N, Λ^N_c, $T^N_{\bar{J}_v}$, have associated stable and unstable (or asymptotic) manifolds of one more dimension than the object itself. The truncated Birkhoff normal form provides an accurate approximation of the local asymptotic manifolds in a neighborhood of L_1. In particular, the 4-dimensional local stable and unstable manifolds of Λ^N_c are given by

$$W^{s,u}_{\text{loc}}(\Lambda^N_c) = \Lambda^N_c \oplus \Upsilon^{s,u},$$

where $\Upsilon^{s,u}$ is a small interval in the stable (unstable) direction. In practice, we take this interval to be of length $\delta = 10^{-3}$; see Section 4.1 for more details.

Once the local stable and unstable manifolds are obtained, the global manifolds are computed by integrating the local ones by the flow Φ_H of (2).

2.3. Scattering map

One of the main tools that we use in this paper is the scattering map. This is an effective tool to quantify the effect of homoclinic excursions to a NHIM. In general, it can be computed either perturbatively or numerically.

We recall the definition of the scattering map following [4]. We consider a general setting of flow Φ on a manifold M, and assume that there is a normally hyperbolic invariant manifold Λ for the flow. We will assume that the flow as well as the geometric objects referred to below are differentiable enough, without formulating specific assumptions on regularity. (In the case of the spatial circular RTBP the flow is real analytic, and the geometric objects of interest are at least C^1-differentiable, but not necessarily analytic.)

As a consequence of normal hyperbolicity, the stable manifold $W^s(\Lambda)$ and the unstable manifold $W^u(\Lambda)$ are foliated by stable and unstable manifolds of points $W^s(y)$, $W^u(y)$, respectively, for $y \in \Lambda$. This implies that for each $x \in W^u(\Lambda)$ there exists a unique $x_- \in \Lambda$ such that $x \in W^u(x_-)$, and for each $x \in W^s(\Lambda)$ there exists a unique $x_+ \in \Lambda$ such that $x \in W^s(x_+)$. These correspondences are described via the *wave maps* $\Omega_+ : W^s(\Lambda) \to \Lambda$ given by $\Omega_+(x) = x_+$, and $\Omega_- : W^u(\Lambda) \to \Lambda$ given by $\Omega_-(x) = x_-$, respectively.

Assume the following transversality conditions:

- $W^s(\Lambda)$ and $W^u(\Lambda)$ intersect transversally along a homoclinic manifold Γ;
- The homoclinic manifold Γ is transverse to the stable (unstable) foliation $\{W^{s,u}_x\}_{x\in\Lambda}$ relative to $W^{s,u}(\Lambda)$.

Then, the restrictions Ω^Γ_+, Ω^Γ_- of Ω_+, Ω_-, respectively, to Γ are local diffeomorphisms. We can always choose Γ so that Ω^Γ_+, Ω^Γ_- are diffeomorphisms onto their images. A homoclinic manifold Γ for which the corresponding restrictions of the wave maps to Γ are diffeomorphisms is referred to as a *homoclinic channel*.

Definition 2.1. *Given a homoclinic channel Γ, the scattering map associated to Γ is the diffeomorphism*

$$S^\Gamma = \Omega^\Gamma_+ \circ (\Omega^\Gamma_-)^{-1}$$

from the $\text{Dom}(S^\Gamma) := \Omega^\Gamma_-(\Gamma) \subseteq \Lambda$ *to the* $\text{Im}(S^\Gamma) := \Omega^\Gamma_+(\Gamma) \subseteq \Lambda$.

That is, if $x \in \Gamma$ is a homoclinic point and $\Omega^\Gamma_\pm(x) = x_\pm$, then $S^\Gamma(x_-) = x_+$. In general, the domain and range of the scattering map are proper subsets of Λ. There are examples where the local domain of the scattering map cannot be extended to a global one, that is, on the whole Λ, as moving along a loop in Λ leads to lack of monodromy (see Delshams et al. [1]).

The scattering map depends on the choice of the homoclinic channel Γ. When we flow the homoclinic channel Γ to $\Phi^t(\Gamma)$, the corresponding scattering maps are conjugate by the flow (see Delshams et al. [4, Section 2.3]):

$$S^{\Phi^t(\Gamma)} = \Phi^t \circ S^\Gamma \circ \Phi^{-t}. \tag{5}$$

Of course, when Γ and $\Phi^t(\Gamma)$ overlap, for $x \in \Gamma \cap \Phi^t(\Gamma)$, we have $S^{\Phi^t(\Gamma)}(x_-) = S^\Gamma(x_-)$. This means that S^Γ can be continued to $S^{\Phi^t(\Gamma)}$ for some interval of times t, for as long as the corresponding homoclinic channels are well defined and can be continued into one another. We will regard the result of such continuation to the maximal domain as a single scattering map.

When the choice of the homoclinic channel Γ is evident from the context, we drop the superscript from the notation S^Γ.

In the case of a discrete-time dynamical system, the scattering map can be defined in a similar fashion.

A remarkable property of the scattering map is that it is exact symplectic, provided that the manifold and the flow are exact symplectic. We refer to Delshams et al. [4] for details.

Remark 1. As we shall see in Section 4.5, in our model we can construct two scattering maps that are defined on a whole annulus inside the NHIM. In this sense, the scattering maps are globally defined on the annulus. Each of this scattering maps is obtained by a continuation of a locally defined scattering map to a maximal domain. In our model, the scattering map extended to its maximal domain satisfies the monodromy condition, as moving around on a non-trivial loop inside the annulus does not yield a multi-valued map.

2.4. Transition map

Assume the general setting from Section 2.3.

From the definition of the scattering map associated to Φ^t, it follows that, if $x \in \Gamma$ is a homoclinic point and

$$S(x_-) = x_+, \text{ where } x_\pm \in \Lambda,$$

then

$$d\left(\Phi^{-t_-}(x), \Phi^{-t_-}(x_-)\right) \to 0, \text{ as } t_- \to \infty,$$
$$d\left(\Phi^{t_+}(x), \Phi^{t_+}(x_+)\right) \to 0, \text{ as } t_+ \to \infty.$$

This correspondence represents the so-called *transition map* (see Delshams et al. [5])).

Definition 2.2. *Given $\delta > 0$, let $T_- = T_-(\delta)$, $T_+ = T_+(\delta)$ be the infimum of the positive reals t_-, t_+, respectively, for which*

$$d\left(\Phi^{-t_-}(x), \Phi^{-t_-}(x_-)\right) \le \delta, \quad d\left(\Phi^{t_+}(x), \Phi^{t_+}(x_+)\right) \le \delta. \tag{6}$$

Then the transition map $\mathcal{T}_\delta : \Phi^{-T_-}(Dom(S)) \to \Phi^{T_+}(Im(S))$ *is defined as*

$$\mathcal{T}_\delta = \Phi^{T_+} \circ S \circ \Phi^{T_-}.$$

The transition map depends on the choice of the homoclinic channel Γ and on the distance δ to the NHIM.

Thus, for T_-, T_+ large enough, the homoclinic orbit segment $\Phi^{[-T_-,T_+]}(x) = \{\Phi^t(x) \,|\, t \in [T_-, T_+]\}$ in M is an approximation of the pseudo-orbit $\Phi^{T_+} \circ S \circ \Phi^{T_-}(x_-)$. The former is an orbit segment in the manifold M, while the latter is given by an orbit segment of the inner dynamics $\Phi^{T_-}{}_{|\Lambda}$, followed by one application of the scattering map S, followed by another orbit segment of the inner dynamics $\Phi^{T_+}{}_{|\Lambda}$.

Remark 2. Note that, for the computation of both the scattering map and the transition map, one needs to know the inner dynamics, given by the restriction to the NHIM. Compared to the scattering map, the transition map depends on an extra parameter (the threshold distance δ to the NHIM), and so, different choices of this parameter yield different transition maps.

Remark 3. In the setting of Section 2.1, we can consider the dynamics of the original flow Φ_H of the RTBP, and the dynamics of the flow Φ_N associated to the Birkhoff normal form, as well as the corresponding NHIMs Λ_c and Λ_c^N, respectively. In each case, we can define a scattering map and a transition map. We denote by S the scattering map corresponding to Φ_H, and by S^N the scattering map corresponding to Φ_N. The map S is defined on some domain in Λ_c, and S^N is defined on some domain in Λ_c^N. Similarly, we denote by $\mathcal{T}_\delta$ the transition map associated to Φ_H, and by $\mathcal{T}_\delta^N$ the transition map associated to Φ_N.

2.5. Reduction of the scattering map and the transition map to a Poincaré section

We now consider the setting from Section 2.1.

In our previous paper [7], we showed that, in the case of the spatial circular RTBP, the unstable and stable manifolds of Λ_c^N intersect, giving rise to homoclinic orbits to Λ_c^N. We can select a homoclinic channel Γ_c and consider the scattering map associated to the truncated Birkhoff normal form:

$$S^N : \mathrm{Dom}(S^N) \subseteq \Lambda_c^N \to \mathrm{Im}(S^N) \subseteq \Lambda_c^N.$$

To reduce the dimensionality of the scattering map, we consider the Poincaré section $\Sigma = \{\phi_p = 0\}$, with associated first return map $\mathcal{F} : \Sigma \to \Sigma$. Let $\Lambda_c^{N,\Sigma}$ denote the intersection of the NHIM with the Poincaré section:

$$\Lambda_c^{N,\Sigma} = \Lambda_c^N \cap \Sigma.$$

We have shown in Delshams et al. [7, Section 3.2] that $\Lambda_c^{N,\Sigma}$ is a normally hyperbolic invariant manifold for $\mathcal{F}$, which we call the *reduced NHIM*. This is a 2-dimensional manifold, that can be parameterized in terms of (J_v, ϕ_v). It has a symplectic structure given by $dJ_v \wedge d\phi_v$. The scattering map induces a *reduced scattering map*:

$$\sigma^N : \mathrm{Dom}(\sigma^N) \subseteq \Lambda_c^{N,\Sigma} \to \mathrm{Im}(\sigma^N) \subseteq \Lambda_c^{N,\Sigma}.$$

The reduced scattering map σ^N is exact symplectic (See Delshams et al. [4]).

Inside $\Lambda_c^{N,\Sigma}$ we consider an annulus given by

$$\mathcal{A} = \Lambda_c^{N,\Sigma} \cap \{\, J_v \in [J_1, J_2],\ \phi_v \in [0, 2\pi)\}$$

where $J_1 < J_2$ will be specified in Section 4.5.

For each fixed value of $J_v = \bar{J}_v$ in the range, there is a unique invariant curve for $\mathcal{F}$

$$T_{\bar{J}}^{N,\Sigma} = \mathcal{A} \cap \{J_v = \bar{J}_v\}.$$

One can derive the reduced scattering map σ from the full scattering map S^N as follows. Let $x_\pm$ be two points related by the scattering map: $x_+ = S^N(x_-)$. Then we flow x_- backwards to the Poincaré section Σ, obtaining a new point $(J_-, \phi_-) \in \Lambda_c^{N,\Sigma}$. Similarly, we flow x_+ forward to Σ, obtaining $(J_+, \phi_+) \in \Lambda_c^{N,\Sigma}$. The reduced scattering map σ^N takes (J_-, ϕ_-) to (J_+, ϕ_+).

When it is clear from the context, we will abbreviate 'reduced scattering map' to just 'scattering map'. Also, for ease of notation, we will simply write (J, ϕ) for (J_v, ϕ_v).

The transition map can be reduced to a surface of section in a similar fashion. Let $x \in \Gamma_c^\Sigma = \Gamma_c \cap \Sigma$ be a homoclinic point and

$$\sigma^N(x_-) = x_+, \text{ where } x_\pm \in \Lambda_c^\Sigma.$$

In terms of the (J, ϕ) coordinates we can write $x_- = (J_-, \phi_-)$ and $x_+ = (J_+, \phi_+)$. For a given $\delta > 0$ where the Birkhoff normal form applies (see Section 4.1), let K_-, K_+ be the smallest positive integers k_-, k_+, respectively, such that

$$d\left(\mathcal{F}^{-k_-}(x), \mathcal{F}^{-k_-}(x_-)\right) < \delta, \quad d\left(\mathcal{F}^{k_+}(x), \mathcal{F}^{k_+}(x_+)\right) < \delta. \tag{7}$$

Then the transition map is given by

$$\tau_\delta^N = \mathcal{F}^{K_+} \circ \sigma^N \circ \mathcal{F}^{K_-}.$$

Remark 4. Since the dynamics along the hyperbolic manifolds $W^{u,s}(\Lambda_c^\Sigma)$ is much faster then the inner dynamics $\mathcal{F}_{|\Lambda_c^\Sigma}$, it may happen that condition (7) is satisfied for $K_- = K_+ = 1$. In that case, the transition map is given by

$$\tau_\delta^N = \mathcal{F} \circ \sigma^N \circ \mathcal{F}.$$

Indeed, the transition map used in this paper will be of this type.

3. Main results

In this section we first provide an abstract result for an iterated function system (IFS) consisting of an inner map (given by the restriction of the dynamics to a NHIM) and finitely many scattering maps, saying that, if the IFS satisfies some verifiable, quantitative conditions, then the system has true 'diffusing' orbits. Then, we give the main numerical result of the paper, which amounts to the numerical verification of the assumptions of the abstract result.

Theorem 1. Assume that $\mathcal{F} : \Sigma \to \Sigma$ is a diffeomorphism on a manifold Σ, Λ is a 2-dimensional NHIM for $\mathcal{F}$, (I, ϕ) a coordinate system on Λ, $\omega = dI \wedge d\phi$ a symplectic form on Λ, and

$$\mathcal{A} = [I_1, I_2] \times \mathbb{T}^1 \subset \Lambda.$$

Assume that $W^s(\mathcal{A})$ and $W^u(\mathcal{A})$ intersect along a homoclinic channel Γ_i, $i \in \{1, \dots, L\}$, where $L \geq 1$. Let $f = \mathcal{F}_{|\mathcal{A}}$ be the restriction of $\mathcal{F}$ to Λ and σ_i be the scattering map associated to Γ_i, $i \in \{1, \dots, L\}$.

I. We assume that the inner map f satisfies the following conditions:

(I.i) The map f is an exact symplectic[1] twist map, i.e.

$$\frac{\partial \pi_\phi f}{\partial I}(I, \phi) > 0. \tag{8}$$

(I.ii) There exists $\rho_1 > 0$ such that for every $\bar{I} \in [I_1, I_2]$, the level set $\{I = \bar{I}\}$ is invariant under f up to an error of ρ_1, that is, for all $n \geq 0$ and $\bar{\phi} \in [0, 2\pi)$, we have

$$|\pi_I(f^n(\bar{I}, \bar{\phi})) - \bar{I}| < \rho_1.$$

II. We assume that each scattering map σ_i, $i \in \{1, \dots, L\}$, satisfies the following conditions:

(II.i) σ_i is globally defined on $\mathcal{A}$, i.e., $\mathrm{dom}(\sigma) \supset \mathcal{A}$;

(II.ii) There exist C^1-functions $\widetilde{\mathcal{L}}_i = \widetilde{\mathcal{L}}_i(I, \phi')$ and $\omega_i = \omega_i(I)$ such that

$$\begin{aligned} I' &= I + \frac{\partial \widetilde{\mathcal{L}}_i}{\partial \phi'}(I, \phi'), \\ \phi &= \phi' + \omega_i(I) + \frac{\partial \widetilde{\mathcal{L}}_i}{\partial \phi'}(I, \phi'), \end{aligned} \tag{9}$$

where we denote $\sigma_i(I, \phi) = (I', \phi')$;

(II.iii) There exists $\rho_2 > \rho_1$ such that for every $\bar{I} \in [I_1, I_2]$ there exists $i \in \{1, \dots, L\}$ and $\bar{\phi} \in [0, 2\pi)$ such that

$$\frac{\partial \widetilde{\mathcal{L}}_i}{\partial \bar{\phi}'}(\bar{I}, \bar{\phi}') > \rho_2. \tag{10}$$

[1] A map f on $\mathcal{A}$ is exact symplectic if $f^*(I d\phi) - I d\phi = ds$ for some function s on $\mathcal{A}$.

Then, for any neighborhood U_1 of $\{I_1\}\times\mathbb{T}^1$ and U_2 of $\{I_2\}\times\mathbb{T}^1$ in Σ there exists an orbit $\{z_n\}_{n=0,\dots,N}$ of $\mathcal{F}$ in Σ such that

$$z_0 \in U_1 \text{ and } z_N \in U_2.$$

Proof. The proof follows immediately from the following result in Moeckel [42], and its extensions in Le Calvez [43] and Gidea and Marco [28]. □

Theorem 2 ([42]). Let $\mathcal{A}=[0,1]\times\mathbb{T}^1$ and $f,g:\mathcal{A}\to\mathcal{A}$ be two C^1-diffeomorphisms of the annulus that preserve the boundary circles.

Assume the following

(i) f is a twist map;
(ii) g is an area preserving map;
(iii) Every essential[2] f-invariant circle Γ is not invariant under g.

Then, for every pair of open neighborhoods U_0 of $\{0\}\times\mathbb{T}$ and U_1 of $\{1\}\times\mathbb{T}$ in $\mathcal{A}$, there exists an orbit $(x_n)_{n=0,\dots,N}$ of the IFS generated by $\{f,g\}$ such that $x_0\in U_0$ and $x_N\in U_1$ (the orbit of the IFS is defined at every step by a choice $x_{n+1}=f(x_n)$ or $x_{n+1}=g(x_n)$).

In Theorem 2 it is essential that the map g is globally defined on the annulus $\mathcal{A}$. On the other hand, the condition that f preserves the boundary components of the annulus can be replaced by the condition that f is exact symplectic. Also, the conditions that g preserves the boundary components of the annulus and that it does not preserve any essential f-invariant circle can be replaced by the condition that for any essential f-invariant circle, there are points below the circle that are mapped by g to points above the circle.

The theorem extends immediately when instead of a single map g we have finitely many maps $g_1,\dots,g_L$ satisfying (ii) such that every essential f-invariant circle Γ is not invariant under some g_i, $i\in\{1,\dots,L\}$.

Condition (I.i) of Theorem 1 in f represents condition (i) of Theorem 2. Condition (II.i) on σ_i from Theorem 1 ensure that these maps are globally defined on $\mathcal{A}$.

Condition (I.ii) of Theorem 1 implies that each essential invariant circle for f is contained within ρ_1 of some I-level set. Conditions (II.ii) and (II.iii) of Theorem 1 imply that for each I-level set, there is a scattering map σ_i and a point on the I-level set whose I-coordinate is increased by σ_i by more than $\rho_2>\rho_1$. Therefore, any essential f-invariant circle fails to remain invariant under at least one of the σ_i. Theorem 2 implies that there is a pseudo-orbit $(x_n)_{n=0,\dots,N}$ of the IFS generated by $\{f,\sigma_1,\dots,\sigma_L\}$ such that $x_0\in U_0$ and $x_N\in U_1$. To obtain a true orbit, we use the following result that follows directly from Gidea et al. [44, Lemma 3.2 and Theorem 3.7].

Theorem 3. Assume that (Σ,ω) is a symplectic manifold of finite symplectic volume, $\mathcal{F}:\Sigma\to\Sigma$ is a symplectic diffeomorphism, $\Lambda\subseteq M$ is a NHIM for $\mathcal{F}$, $f=\mathcal{F}_{|\Lambda}$ and σ_i, $i=1,\dots,L$, is a family of scattering maps on Λ.

Then every finite pseudo-orbit $\{x_i\}_{i=0,\dots,N}$ of the IFS generated by $\{f,\sigma_1,\dots,\sigma_L\}$ in Λ can be shadowed by a true orbit, that is, for every $\delta>0$, there exists an orbit $\{z_i\}_{i=0,\dots,N}$ of $\mathcal{F}$ in Σ, with $z_{i+1}=f^{k_i}(z_i)$ for some $k_i>0$, such that $d(z_i,x_i)<\delta$ for all $i=0,\dots,N$.

Applying Theorem 3 to the $(x_n)_{n=0,\dots,N}$ of the IFS generated by $\{f,\sigma_1,\dots,\sigma_L\}$ yields a true orbit of $\mathcal{F}$ from U_0 to U_1.

We now provide an outline of the numerical verification of the conditions of Theorem 1. Details are provided in Section 10.

Numerical Result 1. *Consider the setting from Section 2.1.*

(a) In Section 4 we obtain the approximation of the NHIM Λ_c by Λ_c^N, using the Birkhoff normal form $H^{(N)}_{trunc}$.
(b) In Section 4.1 we show that the error in the numerical approximation of the NHIM is less than 10^{-15} (close to machine precision).
(c) In Section 4.4 we construct two scattering maps that are globally defined on an annular $\mathcal{A}$ inside Λ_c^N, corresponding to the range $J\in[J_1,J_2]$, where $J_1=0.001$ and $J_2=0.007$. See Section 4.5 for additional details.
(d) In Section 5 we rescale $I=10^3\cdot J$ and derive series representations of the two scattering maps, which are of the form (9).
(e) In Section 6 we show that the generating functions $\widetilde{\mathcal{L}}_i$ associated to these scattering maps satisfy condition (10) for $\rho_2=0.1$. By (b), the level sets of I are preserved by the inner map up to an error of $\rho_1=10^{-12}$.
(f) In Section 7 we verify that the inner map satisfies a twist condition.

Provided that the conditions (a)–(f) have been verified, then there exists a true, zero-cost orbit of Φ_H along which I changes from $I_1=1$ to $I_2=7$.

Remark 5. A result similar to Theorem 1 can be formulated in terms of scattering maps only (without using the inner map). More precisely, assume that we have a family of scattering maps $\{\sigma_1,\dots,\sigma_L\}$ as in Theorem 1, and that one of them, say σ_1, satisfies a twist condition as in (8). Also assume that there exist $0<\rho_1<\rho_2$ such that

$$\max_{\bar\phi'}\left|\frac{\partial\widetilde{\mathcal{L}}_1}{\partial\bar\phi'}(\bar I,\bar\phi')\right|<\rho_1,$$

and for each $\bar I$ there exists $i\neq 1$ such that

$$\max_{\bar\phi'}\frac{\partial\widetilde{\mathcal{L}}_i}{\partial\bar\phi'}(\bar I,\bar\phi')>\rho_2.$$

Then there exist an orbit $\{z_n\}_{n=0,\dots,N}$ of $\mathcal{F}$ as in the conclusion of Theorem 1.

The main idea is that σ_1 plays the role of the inner dynamics in Theorem 1.

[2] An essential circle is a simple closed C^0-curve in $\mathcal{A}$ that is nonhomotopic to zero.

In Sections 4–12 below, we compute numerically the flow Φ_N, the corresponding NHIM Λ_c^N, two scattering maps and two transition maps, as well as their reductions to the surface of section Σ. In Section 4.1 we give an estimate of the error between the original flow Φ_H and the flow computed via the Birkhoff normal form Φ_N, obtaining that Λ_c^N is an accurate enough numerical approximation of Λ_c. As all subsequent computations are performed via the Birkhoff normal form, to simplify the notation, from now on we drop the superscript/subscript N from the notation for all objects.

4. Numerical scattering map on a grid for $C = 3.00088$

Using the methodology presented in our previous paper [7], we compute the NHIM Λ_c and its stable/unstable manifolds. We show that the asymptotic manifolds intersect transversally along two homoclinic channels, giving rise to two different scattering maps. We compute the scattering maps numerically at a grid of points; they are shown in Fig. 9.

For the purpose of this paper we will use the energy value $C = c := 3.00088$. This value is chosen after the appearance of the equilibrium point L_1 ($c_1 := 3.00090$), but before the appearance of *halo* orbits ($c_{\text{halo}} := 3.00082$). The choice of energy is motivated by two reasons.

Firstly, c is close enough to c_1 so that the dynamics around L_1 is almost integrable. Thus, the (integrable) Birkhoff normal form $H^{(N)}_{\text{trunc}}$ provides a good approximation to the local dynamics. (Section 4.1 quantifies the Birkhoff normal form error).

Secondly, c is close enough to c_1 so that we are in the setting of *a priori chaotic Arnold diffusion* (see Section 1).

Fixing the energy value $c = 3.00088$, the NHIM Λ_c consists of a continuous family of 2-dimensional invariant tori around L_1, which we parametrize by the vertical action J. The vertical action increases along the family from $J = 0$ to $J = J_{\max} := 0.052$. Correspondingly, the planar action J_p decreases from 0.05029 to 0.

Fig. 3 shows some tori in the NHIM Λ_c.

- $J = 0$ (i.e. $J_p = 0.05029$) corresponds to the unique planar Lyapunov orbit in this energy level.
- $J = 0.052$ (i.e. $J_p = 0$) corresponds to the unique vertical Lyapunov orbit in this energy level.
- Every intermediate action $J \in (0, 0.052)$ corresponds to a 2-dimensional torus located between the planar and the vertical Lyapunov orbits.

As seen in Fig. 3, the NHIM Λ_c spans a spherical region of radius 0.002 Astronomical Units (AU), or roughly 300,000 km around the equilibrium point L_1.

4.1. Accuracy of the Birkhoff normal form

The accuracy of the Birkhoff normal form (BNF) expansion has been tested against numerical integration of the RTBP equations, following the same procedure as in Jorba and Masdemont [39]. Compute an initial condition on Λ_c by evaluating the BNF up to order $N = 16$. This initial condition is integrated for π units of adimensional time using two different methods:

1. Using the BNF. No numerical integration is needed. As the Hamiltonian is integrable, and we have it integrated, we simply tabulate the solution at time π.

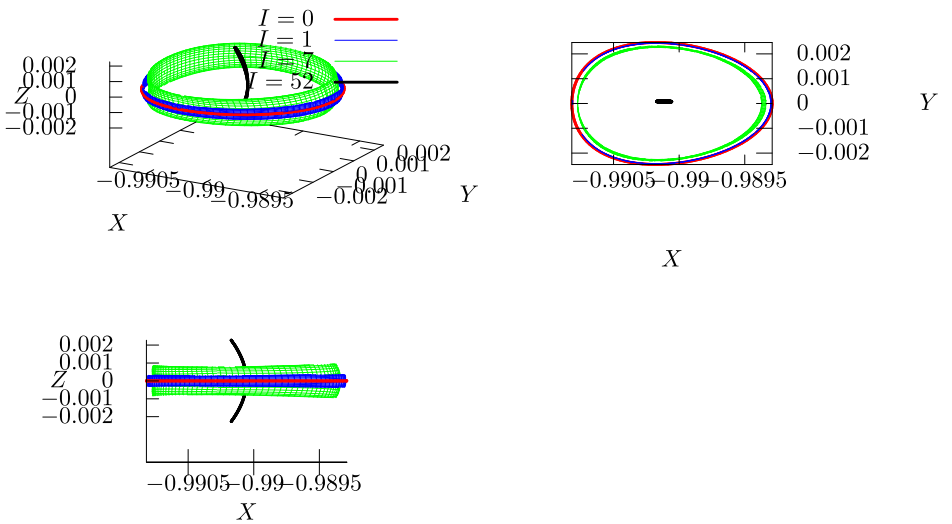

Fig. 3. The NHIM Λ_c consists of a continuous family of invariant tori around L_1. The endpoints of the family are the planar and vertical Lyapunov orbits (shown in red and black, respectively). In between, there are 2-d tori of increasing vertical amplitude J. (For clarity, only two of them are shown). The transfer trajectory shown in Fig. 1 starts at an initial condition very close to the blue torus $I = 1$ and ends very close to the green torus $I = 7$, where $I = 10^3 \cdot J$.

2. Integrate the RTBP equations using a Runge-Kutta-Feldberg numerical integrator of order 7–8, with local error at each step within 10^{-14}.

Then compare the two final conditions.

This test has been performed for several initial conditions on Λ_c. In all cases, the difference in the Euclidean norm for the final condition is less than 10^{-12} adimensional RTBP units. Thus the initial condition was very accurate, in the sense that it is very close to one of the tori computed by the BNF.

In fact, it is known that, due to the hyperbolicity of orbits around the collinear point, errors increase by a factor close to 1500 after π units of time. Therefore the error in the initial condition is less than $10^{-12}/1500$ adimensional units, close to machine precision.

Furthermore, this validity and accuracy of the BNF of order N in a neighborhood of size δ along the unstable/stable coordinates, say for $\delta = 10^{-3}$ and $N = 16$, can also be analytically corroborated using theoretical results, for example from Delshams and Gutiérrez [45]. The bound of the error in a neighborhood of the libration point is there given as a function of the bounds of the Taylor expansion of the Hamiltonian, as well as of the small divisors $k_{\mathrm{p}}\nu_{\mathrm{p}} + k_{\mathrm{v}}\nu_{\mathrm{v}}$ for integers satisfying $|k_{\mathrm{p}}| + |k_{\mathrm{v}}| \leq N$.

It should be noted that the presence of these small divisors is what affects the convergence of these Birkhoff normal forms. Although they depend on the mass ratio μ, they do so very slightly for libration points; see, for instance, Jorba and Masdemont [39], Jorba [40]. Therefore, their influence in detecting strong resonances is not noticeable up to normal form orders much higher than $N = 16$.

4.2. Homoclinic orbits

In [7], Section 4.2, we explained in detail how to compute the intersection of the stable and unstable manifolds $W^s(\Lambda_c) \cap W^u(\Lambda_c)$ restricted to the surface of section

$$\mathcal{S} = \{(X, Y, Z, \dot{X}, \dot{Y}, \dot{Z}) \ : \ Y = 0,\ \dot{Y} > 0\}.$$

We find that the asymptotic manifolds do indeed intersect transversally, giving rise to families of homoclinic orbits to the Λ_c. These homoclinics will later be encoded by two scattering maps.

Briefly, the numerical procedure to compute each homoclinic consists of finding two initial conditions y_-, y_+ on the *local* unstable resp. stable manifolds, and a point $x \in \mathcal{S}$ such that: (1) $\Phi_H^t(y_-) = x$; and (2) $\Phi_H^{-s}(y_+) = x$. Then x is a homoclinic point, generating a homoclinic orbit segment from y_- to y_+.

We would like to emphasize some aspects of this computation:

- We consider **only the first intersection** of the stable and unstable manifolds with the surface of section $\mathcal{S}$. The 'primary' homoclinic connections generated in this way travel around the Earth once.
- The initial conditions y_-, y_+ are taken at a distance $\delta = 10^{-3}$ of the NHIM along the unstable/stable coordinates. This guarantees that they are inside the domain where the Birkhoff normal form is accurate.
- At the same time, these initial conditions are sufficiently far from the NHIM so that the homoclinic orbit segment does not wind around L_1 more than once.
- All homoclinics take $5.936738 \leq t + s \leq 6.000688$ time units to go from y_- to y_+. We will refer to $t + s$ as the 'flight time' of the homoclinic. The shortest and longest flight times correspond to the two homoclinics of the Lyapunov orbit. See Fig. 4.

Following the decomposition of Λ_c into invariant tori, we first study homoclinic orbits from each T_J to itself. Later we will study homoclinic orbits from T_J to nearby tori.

- When $J = 0$, the invariant manifolds $W^u(T_0)$ and $W^s(T_0)$ have 2 transverse intersections in the section $\mathcal{S}$. Hence, the planar Lyapunov orbit T_0 has 2 homoclinic connections with itself. See Fig. 4.
- For every fixed $J \in (0, 0.01)$, the invariant manifolds $W^u(T_J)$ and $W^s(T_J)$ have 8 transverse intersections. That is, every torus T_J in this domain has 8 homoclinic connections with itself.
- In contrast, for action values J above 0.01, the invariant manifolds $W^u(T_J)$ and $W^s(T_J)$ cease to intersect (at their first intersection with the section $\mathcal{S}$).

Remark 6. The planar Lyapunov orbit has two 'primary' homoclinics that travel around the Earth (see Fig. 4). However, one of them makes a longer excursion than the other: the green homoclinic has flight time 5.936738, while the blue one has flight time 6.000688.

Remark 7. Each of the 2 intersections in $W^u(T_0) \cap W^s(T_0)$ gives rise to 4 intersections when we increase the dimension of the manifolds $W^u(T_J), W^s(T_J)$ by one. This is expected by Morse theory [46].

4.3. Computation of local transition map and scattering map

Consider a homoclinic point $x \in \mathcal{S}$ as found in Section 4.2, generating a homoclinic orbit segment from $y_- \in W^u_{loc}(\Lambda_c)$ to $y_+ \in W^s_{loc}(\Lambda_c)$, with flight time $t + s$. Let

$$y_- = \left(y_h^- = \delta, J_p^-, J_v^-, x_h^- = 0, \phi_p^-, \phi_v^-\right)$$

and

$$y_+ = \left(y_h^+ = 0, J_p^+, J_v^+, x_h^+ = \delta, \phi_p^+, \phi_v^+\right)$$

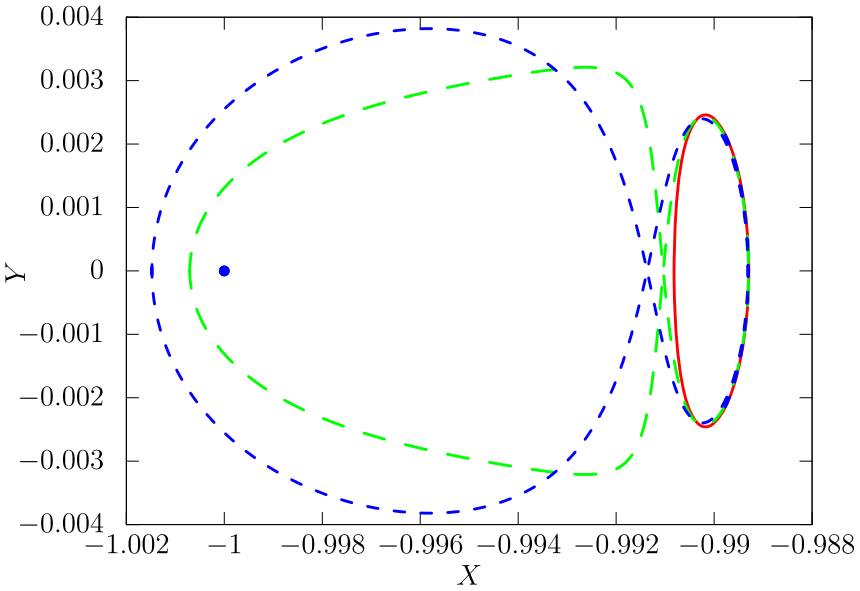

Fig. 4. Planar Lyapunov orbit (solid line), and its two 'primary' homoclinics (dashed). Both homoclinics travel around the Earth once (located at $X = -1 + \mu$).

in Birkhoff normal form coordinates. Then, the transition map $\mathcal{T}_\delta : \ \Lambda_c \to \Lambda_c$ is given by

$$\left(J_p^-, J_v^-, \phi_p^-, \phi_v^-\right) \mapsto \left(J_p^+, J_v^+, \phi_p^+, \phi_v^+\right).$$

As explained in Section 2.4, the scattering map $S : \ \Lambda_c \to \Lambda_c$ is related to the transition map by the flow. Therefore, the scattering map is given by

$$x_- := \Phi^t\left(J_p^-, J_v^-, \phi_p^-, \phi_v^-\right) \mapsto x_+ := \Phi_H^{-s}\left(J_p^+, J_v^+, \phi_p^+, \phi_v^+\right).$$

Every transverse intersection

$$x \in W^u(T_J) \cap W^s(T_J)$$

implies that there exists a pair of points $x_-, x_+ \in T_J$ such that $W^u(x_-)$ intersects $W^s(x_+)$ at the homoclinic point x. Since this is an open condition, we can define a local scattering map on some open set containing x_- by $x_- \mapsto S(x_-) := x_+$.

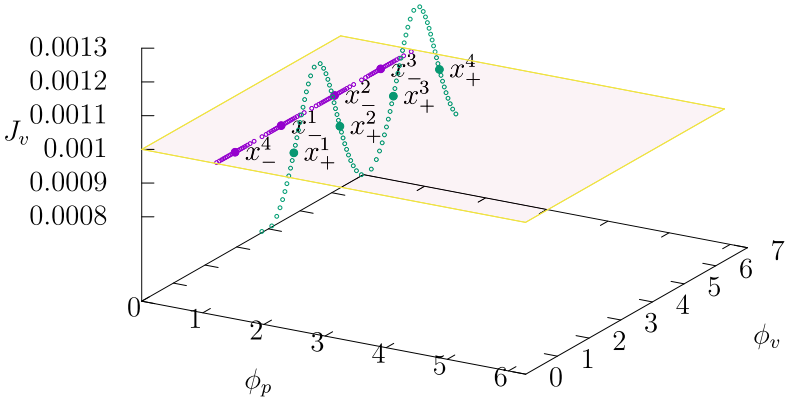

Fig. 5. Action of the scattering map S_1 on the torus T_J with $J = 0.001$. S_1 maps the purple set to the green set. When the 'source' and 'destination' tori T_J have the same action ($J = 0.001$ in this picture, corresponding to the translucent plane), S_1 maps the 4 points $x_-^i \in T_J$ to $x_+^i \in T_J$. Fixing the source torus T_J and varying the destination torus $T_{J'}$ to action levels J' near J, the scattering map S_1 is continued to the purple and green sets.

In fact, we find that these local scattering maps can be continued to form two *global* scattering maps, which we will denote S_1 and S_2. They determine the reduced scattering maps, σ_1 and σ_2 (see Section 2.5).

4.4. Extending the scattering map

Let us explain how S_1 is numerically constructed. (S_2 is constructed analogously). The general idea is to compute S_1 on several tori T_J (for example $J = 0.001, 0.002, \dots, 0.007$). This provides a coarse representation of S_1.

To compute S_1 on a given torus T_J, fix an action $J \in [0.001, 0.007]$. As explained above, $W^u(T_J)$ has 8 transverse intersections with $W^s(T_J)$ in the surface of section $\mathcal{S}$. Four of them, which we will denote x^i for $i = 1, 2, 3, 4$, give rise to 4 pairs of points associated by the local scattering maps:

$$x^i_+ = S(x^i_-) \qquad \text{for } i = 1, \dots, 4.$$

Fig. 5 shows these 4 pairs of points: x^i_- in the domain of S_1 are plotted in purple, while x^i_+ in the codomain are plotted in green.

Keeping the action of the source torus fixed to J, vary the action of the destination torus to a new value J' close to J, and recompute the intersection $W^u(T_J) \cap W^s(T_{J'})$, giving rise to 4 new homoclinic points and 4 corresponding pairs of points associated by S_1. Continue this procedure until the manifolds $W^u(T_J)$ and $W^s(T_{J'})$ cease to intersect, effectively extending the domain of the scattering map S_1 from 4 points to the purple set in Fig. 5, and the codomain to the green set.

Remark 8. Starting with the other 4 homoclinic points, x^i for $i = 5, 6, 7, 8$, and applying the same procedure, gives rise to a different scattering map S_2. See Fig. 6. S_1 and S_2 are fundamentally different, as they are not conjugated by the flow in the sense of (5).

We repeat this procedure for the tori $J = 0.001, 0.002, \dots, 0.007$. See Fig. 7.

Remark 9. For $J \to 0$, the torus T_J degenerates into the horizontal Lyapunov periodic orbit T_0. The 4 homoclinic points x^i converge to a single homoclinic point x for T_0. Similarly, the 4 pairs x^i_-, x^i_+ converge to a single pair x_-, x_+ of points associated by S_1. Fig. 7 shows x_-, x_+ as straight lines (all angles $\phi_v \in [0, 2\pi)$ are identified for $J = 0$).

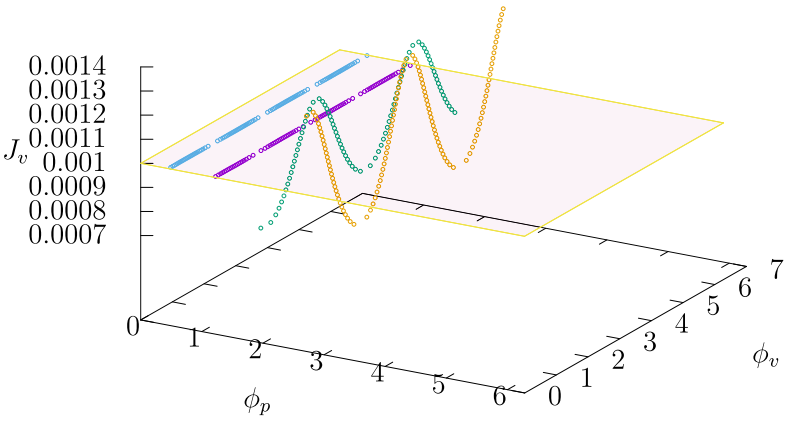

Fig. 6. Action of scattering maps S_1 and S_2 on the torus T_J with $J = 0.001$. S_1 maps the purple set to the green set, while S_2 maps blue to orange.

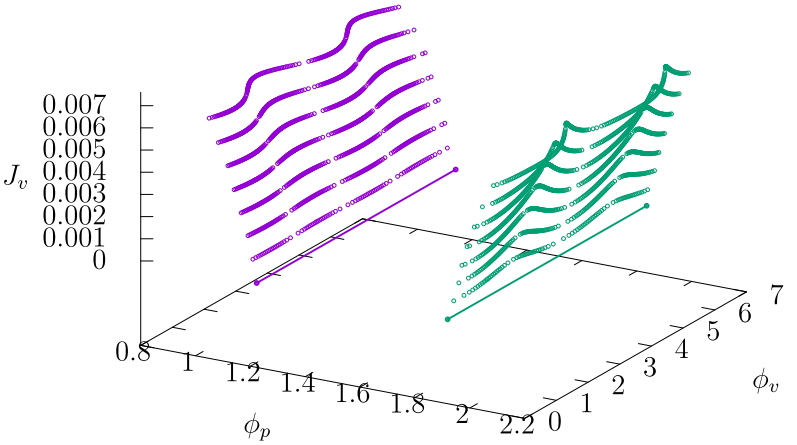

Fig. 7. S_1 acting on several action levels: $J = 0.001, 0.002, \dots, 0.007$.

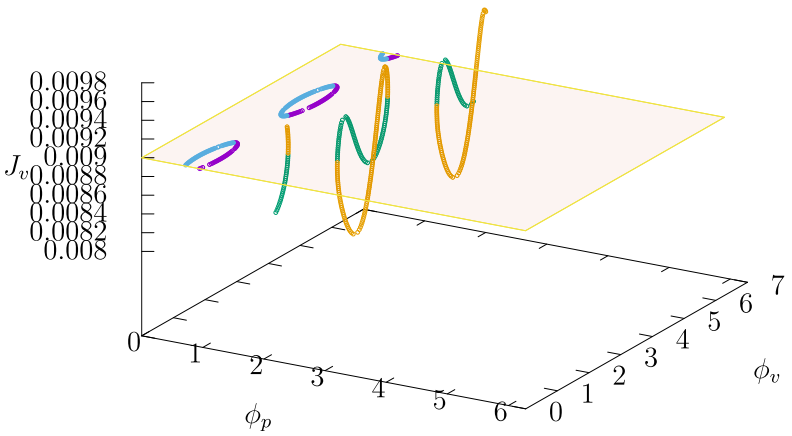

Fig. 8. Action of scattering maps S_1 and S_2 on the action level $J = 0.009$. S_1 and S_2 have 'merged', and they can not be extended to the whole torus.

Using the computation of S_1 we compute the reduced scattering map σ_1. Recall from Section 2.5 that the reduced scattering map can be obtained from the full scattering map simply by flowing the points x_-/x_+ backwards/forwards to the Poincaré section $\Sigma = \{\phi_p = 0\}$.

Flowing the purple set backwards to Σ, we obtain a mesh $\{(J, \phi)\}$ discretizing the reduced NHIM Λ_c^Σ. Flowing the green set forwards to Σ, we obtain the image set $\{(J', \phi')\}$ under σ_1, also on Λ_c^Σ. This way, we have extended the local scattering maps onto a global (reduced) scattering map σ_1 on Λ_c^Σ.

Fig. 9 (top panel) shows the image set of the global scattering map σ_1. For example, the green set in Fig. 5 ($J = 0.001$) corresponds to the lowest curve in Fig. 9 after flowing it forward.

4.5. Domain of the global scattering map

From above, the global scattering maps σ_1, σ_2 are well defined on an annulus $\mathcal{A}$ inside Λ_c^Σ given by

$$\mathcal{A} = \{(J, \phi) : \ J \in [0.001, 0.007] \text{ and } \phi \in [0, 2\pi)\}. \tag{11}$$

For $0.007 < J < 0.01$, we find that the scattering maps can not be defined on the whole torus T_J. For illustration, Fig. 8 shows the continuation of all 8 local scattering maps when $J = 0.009$. Notice that the purple and blue sets (which belong to the domain of S_1 and S_2 respectively) have become connected, and they form two contractible circles. Moreover, the purple and blue sets do not cover all angles $\phi_v \in [0, 2\pi)$ as before. Thus one can not extend S_i to the whole torus T_J by the flow using the conjugacy property (5). Consequently, the reduced scattering map σ_i is not defined on the whole invariant curve T_J^Σ.

For the purpose of this paper, we will restrict the domain of the global scattering maps σ_1, σ_2 to the annulus $\mathcal{A}$.

5. Series representation of the scattering map

The goal of this section is to introduce a series representation of the (global, reduced) scattering maps σ_1 and σ_2. This finite series expansion consists in Eqs. (13)–(15) and (19) below. It is a more efficient representation than the numerical scattering map computed in the previous section, since it is limited to a small number of terms. Moreover, it allows us to evaluate σ_i, $i = 1, 2$, at any point of its domain.

Note that J and ϕ have different scales: J is of order 10^{-3}, while ϕ is of order 1. To improve numerical conditioning, we scale J as follows:

$$I = 1000J. \tag{12}$$

From now on, we will work with the scaled coordinate I instead of J.

The most classical way to represent a symplectic map $(I, \phi) \to (I', \phi')$ is by a generating function depending on old and new variables. In [10], the scattering map on Lyapunov periodic orbits was shown to be a phase shift $(I, \phi) \to (I, \phi + \Delta(I))$. Thus, in our setting it is natural to look for a generating function of the form

$$\mathcal{L}(I, \phi') = I\phi' + \Omega(I) + \widetilde{\mathcal{L}}(I, \phi'),$$

which will at least be valid for small values of I. The generating function $\mathcal{L}(I, \phi')$ is decomposed into its average part with respect to ϕ', denoted $\Omega(I)$, and its oscillatory part $\widetilde{\mathcal{L}}(I, \phi')$, which satisfyies $\int_0^{2\pi} \widetilde{\mathcal{L}}(I, \phi')\mathrm{d}\phi' = 0$.

Hence, the equations for the scattering map $(I', \phi') = \sigma(I, \phi)$ are given implicitly by

$$\phi = \frac{\partial \mathcal{L}}{\partial I}(I, \phi') = \phi' + \omega(I) + \frac{\partial \widetilde{\mathcal{L}}}{\partial I}(I, \phi') \tag{13a}$$

$$I' = \frac{\partial \mathcal{L}}{\partial \phi'}(I, \phi') = I + \frac{\partial \widetilde{\mathcal{L}}}{\partial \phi'}(I, \phi'), \tag{13b}$$

where $\omega(I) = \Omega'(I)$.

We will approximate both $\widetilde{\mathcal{L}}(I, \phi')$ and $\omega(I)$ in Eq. (13) using finite series expansions. Firstly, since we are going to work with few values of I, we approximate the function $\widetilde{\mathcal{L}}(I, \phi')$ using a Fourier-Polynomial interpolation:

$$\widetilde{\mathcal{L}}(I, \phi') = -\sum_{n=1}^{N} \frac{B_n(I)}{n} \cos n\phi' + \sum_{n=1}^{N} \frac{A_n(I)}{n} \sin n\phi', \tag{14}$$

where

$$A_n(I) = \sum_{l=0}^{L} a_l^{(n)} I^l \quad \text{and} \quad B_n(I) = \sum_{l=0}^{L} b_l^{(n)} I^l. \tag{15}$$

The goal is to find the coefficients $a_l^{(n)}$ and $b_l^{(n)}$. In Section 4, we obtained numerically the scattering map σ on a grid of equispaced (I, ϕ) points. See Fig. 9. It is a simple matter to fit the coefficients to this data, as explained in Section 5.1.

Remark 10. The spatial RTBP is invariant with respect to the transformation $(Z, \dot{Z}) \to (-Z, -\dot{Z})$. Thus, every trajectory passing through the point (X, Y, Z) has a *symmetric trajectory with respect to the XY plane*, which passes through the point $(X, Y, -Z)$. In particular, every heteroclinic trajectory from torus I to torus I' has a symmetric heteroclinic trajectory from torus I to I'. In Birkhoff normal form coordinates, the symmetry $Z \to -Z$ corresponds to $\phi_v \to \phi_v + \pi$. This translates to the following fact for the scattering map of the flow. Suppose that $S(J_v, \phi_p, \phi_v) = (J_v', \phi_p', \phi_v')$. Then we have $S(J_v, \phi_p, \phi_v + \pi) = (J_v', \phi_p', \phi_v' + \pi)$. Equivalently for the reduced scattering map: Suppose that $\sigma(I, \phi_v) = (I', \phi_v')$. Then we have $\sigma(I, \phi_v + \pi) = (I', \phi_v' + \pi)$. This implies that the image under the scattering map of any torus is a π-periodic curve (see Fig. 9). Indeed, we have checked that the curves in Fig. 9 are π-periodic up to a tolerance of 10^{-6}. From this point on, **we will plot all figures involving ϕ_v in the domain $[0, \pi)$ only.**

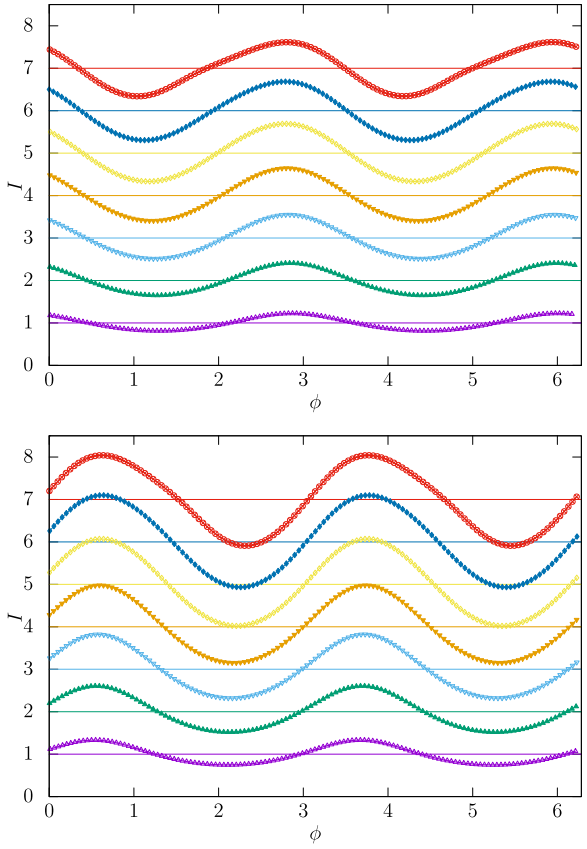

Fig. 9. Image under the scattering map of several tori ($I = 1, 2, \ldots, 7$). Above: action of σ_1, below: action of σ_2. A torus $\{(I, \phi) : I = \text{const}, \phi \in [0, 2\pi)\}$ and its image are plotted using the same color. Notice that the curves are π-periodic.

5.1. Fourier-polynomial interpolation of the generating function

Let I be fixed, and consider Eq. (13b):

$$I' = I + \frac{\partial \widetilde{\mathcal{L}}}{\partial \phi'},$$

where

$$\frac{\partial \widetilde{\mathcal{L}}}{\partial \phi'} = \sum_{n=1}^{N} A_n \cos n\phi' + \sum_{n=1}^{N} B_n \sin n\phi'. \tag{16}$$

Given a set of (I', ϕ') values on a grid (data points composing one curve in Fig. 9), we use the discrete Fourier transform to obtain the Fourier coefficients A_n, B_n.

Remark 11. Since we have 128 (I', ϕ') data points for each torus, the maximum possible degree of the Fourier expansion (14) is $N = 64$.

Next, let I vary to obtain the Fourier coefficients $A_n(I)$, $B_n(I)$ for each torus $I = 1, 2, \dots, 7$. Fig. 10 shows the decay of these Fourier coefficients for each torus.

Remark 12. We know from Remark 10 that the scattering map is π-periodic. Thus, for each torus $I = const$, its image is a π-periodic curve $I' = \gamma(\phi')$, and the odd Fourier coefficients should all be zero: $A_{2k+1}(I) = B_{2k+1}(I) = 0$ for $k = 0, 1, 2, \dots$. Of course, in Fig. 10 they are not exactly zero because the numerical data is not exactly π-periodic. From now on, all odd Fourier coefficients are set to zero, to obtain a model that satisfies the theoretical π-periodicity of the scattering map.

Let now the index n of the Fourier coefficient be fixed, and consider the polynomial approximation of $A_n(I)$ and $B_n(I)$ given in Eq. (15). Alternatively, given a set of $L+1$ data points $(I_0, A_n(I_0)), \dots, (I_L, A_n(I_L))$, we will express the polynomials (15) in Newton's form

$$A_n(I) = \sum_{l=0}^{L} \tilde{a}_l^{(n)} N_l(I) \quad \text{and} \quad B_n(I) = \sum_{l=0}^{L} \tilde{b}_l^{(n)} N_l(I), \tag{17}$$

where $\tilde{a}_l^{(n)}, \tilde{b}_l^{(n)}$ are the *divided differences*, and $N_l(I)$ are Newton's basis polynomials

$$N_0(I) = 1, \quad N_l(I) := \prod_{i=0}^{l-1} (I - I_i) \ \text{ for } l = 1, \dots, L.$$

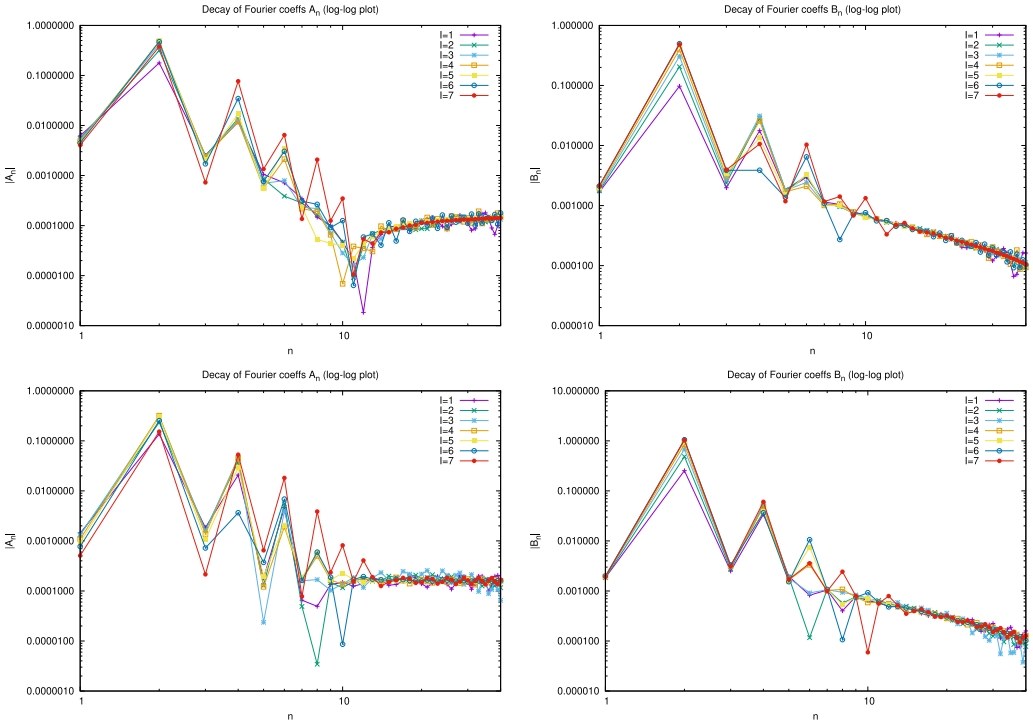

Fig. 10. Decay of Fourier coefficients (log-log plot) for the scattering map σ_1 (above) and σ_2 (below).

Given the values $A_n(I)$ at $I = 0, 1, 2, \dots, 7$ obtained in the previous step (resp. $B_n(I)$), we use polynomial interpolation (Newton's 'divided differences' algorithm) to obtain the coefficients $\tilde{a}_l^{(n)}$ (resp. $\tilde{b}_l^{(n)}$). The divided differences of the first 8 Fourier coefficients are listed in Table 1.

Remark 13. Since we only have 8 data points for each Fourier coefficient, the maximum possible degree of the Newton expansion (17) is $L = 7$.

Remark 14. The constant terms $\tilde{a}_0^{(n)}, \tilde{b}_0^{(n)}$ of the Newton expansion are all zero, since $\tilde{a}_0^{(n)} = A_n(0) = 0$ and $\tilde{b}_0^{(n)} = B_n(0) = 0$ for all n.

5.2. Polynomial interpolation of the frequency $\omega(I)$

Finally, we approximate the frequency $\omega(I)$ in Eq. (13).

5.2.1. Frequency $\omega(I)$ at $I = 1, 2, \dots, 7$

For action levels $I = 1, 2, \dots, 7$ we have available the scattering map data $(I, \phi) \to (I', \phi')$, so the frequency $\omega(I)$ can be obtained from Eq. (13a) as

$$\omega(I) = \phi - \phi' - \frac{\partial \widetilde{\mathcal{L}}}{\partial I}(I, \phi'). \tag{18}$$

In an exact calculation, $\omega(I)$ should be independent of ϕ. Numerically, using Eq. (18) to approximate the value of $\omega(I)$ would yield slightly different values for $\omega(I)$ depending on the data point (I, ϕ), and indeed depending on ϕ. Thus, we will compute $\omega(I)$ as the *average* of Eq. (18) over all $\phi \in [0, 2\pi)$.

5.2.2. Frequency $\omega(I)$ at an arbitrary I-value

Similarly to what we did in Section 5.1 with the Fourier coefficients $A_n(I)$, $B_n(I)$, we use the Newton series representation of $\omega(I)$:

$$\omega(I) = \sum_{l=0}^{L} \tilde{c}_l N_l(I). \tag{19}$$

Table 1
Divided differences $\tilde{a}_l^{(n)}$, $\tilde{b}_l^{(n)}$ of the first Fourier coefficients $A_n(I)$, $B_n(I)$. All odd Fourier coefficients are zero and thus not listed (see Remark 12). All constant terms of the Newton expansion $\tilde{a}_0^{(n)}$, $\tilde{b}_0^{(n)}$ are zero, and thus not listed (see Remark 14). Notice that the two coefficients $\tilde{a}_1^2$ and $\tilde{b}_1^2$ (in red) are much larger than the rest of coefficients for both scattering maps σ_1, σ_2. For the scattering map σ_1, the coefficient $\tilde{a}_2^2$ (in blue) is much larger than the rest of coefficients in the last six columns, i.e. $\tilde{a}_j^n$ for $j \geq 2$. For the scattering map σ_2, the two coefficients $\tilde{a}_2^2$ and $\tilde{b}_2^2$ are much larger than the rest with $j \geq 2$.

n	$\tilde{a}_1^{(n)}$	$\tilde{a}_2^{(n)}$	$\tilde{a}_3^{(n)}$	$\tilde{a}_4^{(n)}$	$\tilde{a}_5^{(n)}$	$\tilde{a}_6^{(n)}$	$\tilde{a}_7^{(n)}$
2	**0.178180**	**-0.020025**	0.000401	-0.000251	0.000046	0.000019	-0.000022
4	0.011726	-0.004878	0.001114	-0.000129	0.000039	-0.000006	0.000001
6	0.000712	-0.000519	0.000295	-0.000065	0.000004	-0.000000	-0.000001
8	0.000147	-0.000064	0.000027	-0.000012	0.000002	0.000000	0.000000
n	$\tilde{b}_1^{(n)}$	$\tilde{b}_2^{(n)}$	$\tilde{b}_3^{(n)}$	$\tilde{b}_4^{(n)}$	$\tilde{b}_5^{(n)}$	$\tilde{b}_6^{(n)}$	$\tilde{b}_7^{(n)}$
2	**-0.097275**	-0.005156	0.002856	-0.000574	0.000143	0.000003	-0.000016
4	-0.017677	0.003403	0.000242	-0.000067	0.000004	-0.000000	-0.000003
6	-0.002965	0.001408	-0.000332	0.000035	-0.000008	0.000002	-0.000000
8	-0.001045	0.000566	-0.000206	0.000053	-0.000009	0.000002	-0.000000

(a) Scattering map σ_1.

n	$\tilde{a}_1^{(n)}$	$\tilde{a}_2^{(n)}$	$\tilde{a}_3^{(n)}$	$\tilde{a}_4^{(n)}$	$\tilde{a}_5^{(n)}$	$\tilde{a}_6^{(n)}$	$\tilde{a}_7^{(n)}$
2	**0.136664**	**-0.019375**	0.001251	-0.001067	0.000499	-0.000153	0.000031
4	-0.020745	0.001757	0.000921	-0.000221	0.000089	-0.000028	0.000006
6	-0.004644	0.001886	-0.000222	-0.000027	-0.000001	0.000001	-0.000000
8	-0.000049	0.000048	-0.000051	0.000015	0.000000	0.000000	-0.000000
n	$\tilde{b}_1^{(n)}$	$\tilde{b}_2^{(n)}$	$\tilde{b}_3^{(n)}$	$\tilde{b}_4^{(n)}$	$\tilde{b}_5^{(n)}$	$\tilde{b}_6^{(n)}$	$\tilde{b}_7^{(n)}$
2	**0.253827**	**-0.011566**	-0.001286	0.000406	-0.000226	0.000067	-0.000018
4	0.034009	-0.008888	0.000925	-0.000160	0.000086	-0.000022	0.000006
6	0.000823	-0.000764	0.000505	-0.000121	0.000025	-0.000008	0.000001
8	0.000400	-0.000113	0.000069	-0.000035	0.000007	0.000000	0.000000

(b) Scattering map σ_2.

Table 2
Divided differences $\tilde{c}_l$ of function $\omega(I)$. Notice that the coefficient $\tilde{c}_0$ (in red) is much larger than the rest of coefficients of this table, and larger than those of Table 1, for both scattering maps σ_1 and σ_2. Notice also that $\tilde{c}_1$ (in blue) is much larger than the rest of coefficients of the last five columns, i.e $\tilde{c}_j$ for $j \geq 2$, of this table, and larger than the double of those coefficients of the last 6 columns of Table 1 for both scattering maps σ_1 and σ_2.

$\tilde{c}_0$	$\tilde{c}_1$	$\tilde{c}_2$	$\tilde{c}_3$	$\tilde{c}_4$	$\tilde{c}_5$	$\tilde{c}_6$
2.027748	**0.046673**	0.001164	0.000489	-0.000046	0.000016	0.000003

(a) Scattering map σ_1.

$\tilde{c}_0$	$\tilde{c}_1$	$\tilde{c}_2$	$\tilde{c}_3$	$\tilde{c}_4$	$\tilde{c}_5$	$\tilde{c}_6$
3.555994	**-0.046434**	-0.001651	-0.000143	-0.000115	0.000046	-0.000026

(b) Scattering map σ_2.

Given the values $\overline{\omega}(I)$ at $I = 1, 2, \ldots, 7$, obtained in the previous step, we use polynomial interpolation to obtain the coefficients $\tilde{c}_l$. The frequency function $\omega(I)$ is plotted in Fig. 11.

Remark 15. Since we only have 7 data points for ω, the maximum possible degree of the Newton expansion (19) is $L = 6$.

This completes the series representation of the scattering map, consisting of Eqs. (14), (15) and (19).

5.3. Applying the scattering map

We will use Eq. (13) to apply the scattering map $(I', \phi') = \sigma(I, \phi)$. Note that (13) give I', ϕ' *implicitly* as functions of I, ϕ. However, ϕ' can be obtained from Eq. (13a) as a fixed point of

$$\phi' = f(\phi'; I, \phi) = \phi - \omega(I) - \frac{\partial \widetilde{\mathcal{L}}}{\partial I}(I, \phi').$$

We simply use fixed point iteration, starting with the initial approximation $\phi'_0 = \phi - \omega(I)$. We require an absolute error smaller than 10^{-5} in the fixed point to stop the iteration. There is no point in requiring higher precision, because the error of our series representation in the angle variable is larger than 10^{-2}; see Table 4 (bottom panel).

Once ϕ' is known, I' is obtained directly from Eq. (13b).

6. Approximation error

Now we have two different representations of the scattering map:

- The **numerical scattering map** $\sigma(I, \phi)$ was obtained in Section 4 using Birkhoff normal forms and numerical continuation of the invariant manifolds. It was calculated on a relatively coarse grid of points (Fig. 9).
- The **standard scattering map (SSM)** $\tilde{\sigma}(I, \phi)$ consists in the Fourier-Polynomial interpolation (14), (15) and (19). The series approximation has been derived in Section 5 from the numerical map, so it is not as precise. However, it has the advantage that it can be evaluated at any desired point (I, ϕ).

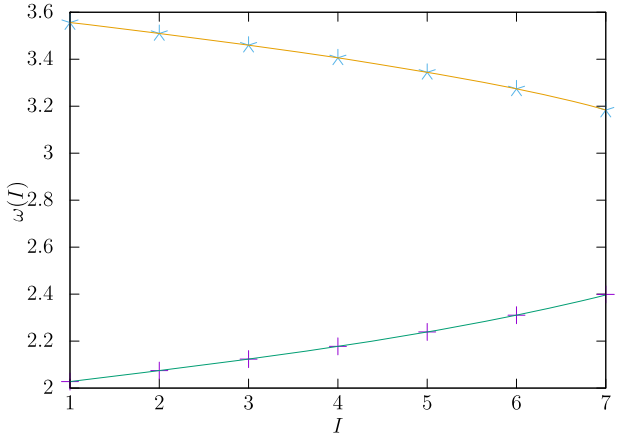

Fig. 11. Frequency function $\omega(I)$ for σ_1 (in green) and σ_2 (yellow).

To measure the quality of the series approximation, we do the following:

1. Read the numerical scattering map from file as a table:

$$(I', \phi') = \sigma(I, \phi).$$

We have its values on a grid of points (I, ϕ).

2. Evaluate the standard scattering map (SSM) *on the same grid*:

$$(\tilde{I}', \tilde{\phi}') = \tilde{\sigma}(I, \phi).$$

3. Find the approximation error, defined as the *maximum over all grid points* of

$$(\epsilon_I, \epsilon_\phi) = \left(|\tilde{I}' - I'|, |\tilde{\phi}' - \phi'|\right).$$

Remark 16. To better test the quality of the series approximation, we also compute the approximation error on a new set of data, independent of the original one. That is, we extend the original data set $I = 1, 2, \dots, 7$, used to derive $\tilde{\sigma}$ with the new data set $I = 0.5, 1.5, 2.5, \dots, 6.5$. See Fig. 12. Thus, only for testing purposes, we use 14 tori. As shown in Tables 4, 5, the errors in the independent data set are comparable to those of the original data set.

Of course, the approximation error depends on the chosen degree (N, L) of the Fourier-Polynomial interpolation. For illustration, Fig. 12 compares the quality of a low order versus a high order approximation.

We will distinguish two different settings. In the *local* setting, one is interested in an accurate representation of the scattering map in a neighborhood of $I = 0$, whereas in the *global* setting, one is interested in an accurate representation in the whole domain of the global scattering map.

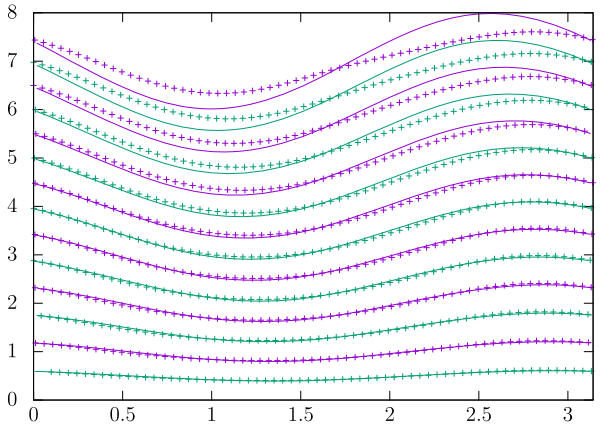

(a) $N = 2, L = 2$

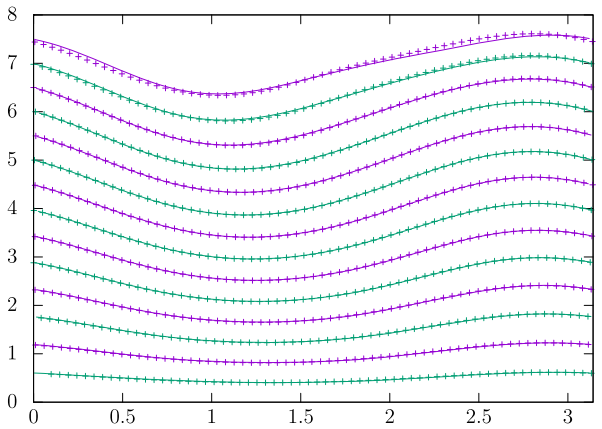

(b) $N = 4, L = 5$

Fig. 12. Image of the numerical scattering map (points) versus the standard scattering map (SSM) of degree N, L (lines). For testing purposes, we check the approximation error both on the original data set $I = 1, 2, \dots, 7$ (in purple) and on the independent data set $I = 0.5, 1.5, 2.5, \dots, 6.5$ (in green).

Table 3
Local approximation error ϵ_I (top panel) and ϵ_ϕ (bottom panel) as a function of N, L for the first scattering map σ_1.

	L			
N	0	1	2	3
2	0.540000	0.134772	0.041698	0.037342
4	0.540000	0.145286	0.019337	0.011640
6	0.540000	0.151078	0.019536	0.013382

	L		
N	0	1	2
2	0.156427	0.052403	0.015123
4	0.156427	0.049706	0.016311
6	0.156427	0.049634	0.016270

6.1. Local approximation error

For definiteness, let us fix the local domain to be

$$\mathcal{A}_{\text{loc}} = \{(I,\phi):\ \ I \in [1,3] \text{ and } \phi \in [0,2\pi)\}.$$

We have computed the approximation error over the local domain $\mathcal{A}_{\text{loc}}$ as a function of the degree (N, L) of the Fourier-Polynomial interpolation; see Table 3.

Remark 17. Only the grid points (I,ϕ) belonging to the local domain (i.e tori $I = 1,2,3$) are used in the computation of the local approximation error.

The error of the Fourier-Polynomial interpolation model decreases as N and L increase, but not monotonically. If we want an approximation error $\epsilon = \max\{\epsilon_I, \epsilon_\phi\}$ less than 0.05, then it is enough to take $N = 2$ and $L = 2$. Notice that the improvement is mild beyond that point. Indeed, Fig. 12(a) shows that $N = L = 2$ gives a good approximation in the local domain $\mathcal{A}_{\text{loc}}$.

Thus, it is natural to choose $N = L = 2$ to obtain an accurate model for the local scattering map. In fact, as discussed before (Remark 12), we neglect the odd Fourier coefficients $A_1(I)$ and $B_1(I)$ due to the symmetry of the problem, and just keep the even ones $A_2(I)$ and $B_2(I)$.

Therefore, in the local setting, an **accurate model** for the scattering map is given by the Fourier-Polynomial interpolation

$$\widetilde{\mathcal{L}}(I,\phi') = -\frac{B_2(I)}{2}\cos 2\phi' + \frac{A_2(I)}{2}\sin 2\phi',$$

where

$$A_2(I) = \tilde{a}_0^{(2)} + \tilde{a}_1^{(2)} I + \tilde{a}_2^{(2)} I(I-1)$$
$$B_2(I) = \tilde{b}_0^{(2)} + \tilde{b}_1^{(2)} I + \tilde{b}_2^{(2)} I(I-1),$$

$$\omega(I) = \tilde{c}_0 + \tilde{c}_1(I-1) + \tilde{c}_2(I-1)(I-2),$$

are polynomials of degree 2 in I, determined by only 9 coefficients. These coefficients were given in Tables 1 and 2.

This part of the generating function can also be written as $\widetilde{\mathcal{L}}(I,\phi') = C_2(I)\cos\left(2\phi' - 2\phi'_0\right)$, a cosine function of period π at angle ϕ'. The corresponding Standard Scattering Map (SSM) can thus be used as a universal local model around saddle-center libration points of the RTBP problem, and its cosine expression explains the shape of the KAM curves in Fig. 14.

6.2. Global approximation error

Suppose now that we are now interested in an accurate representation in the whole domain of the scattering map

$$\mathcal{A} = \{(I,\phi):\ \ I \in [1,7] \text{ and } \phi \in [0,2\pi)\}. \tag{20}$$

The approximation error over the global domain is given in Table 4. If we want an approximation error $\epsilon = \max\{\epsilon_I, \epsilon_\phi\}$ less than 0.1, we need to increase the degree of Fourier-Polynomial interpolation to $N = 4$ and $L = 5$. In fact, Fig. 12(b) shows that $N = 4,\ L = 5$ gives a good approximation in the global domain $\mathcal{A}$.

From now on, we will use $N = 4,\ L = 5$ as our model for the global scattering map σ_1.

A similar analysis suggests that $N = 4,\ L = 6$ be used for the global scattering map σ_2.

Table 4
Global approximation error ϵ_I (top panel) and ϵ_ϕ (bottom panel) as a function of N, L for the standard scattering map σ_1. The error is evaluated in the original data set $I = 1, 2, \dots, 7$.

	L							
N	0	1	2	3	4	5	6	7
2	0.680000	0.963414	0.495653	0.261042	0.385496	0.131751	0.219163	0.094550
4	0.680000	0.975219	0.618115	0.276085	0.387552	0.087317	0.156552	0.021123
6	0.680000	0.996139	0.656461	0.266668	0.381078	0.107612	0.144998	0.013382
8	0.680000	1.003501	0.657922	0.287596	0.367730	0.110813	0.148937	0.013159
10	0.680000	1.007927	0.647908	0.287781	0.356098	0.105846	0.149545	0.012512

	L						
N	0	1	2	3	4	5	6
2	0.449508	0.268271	0.157380	0.065119	0.148788	0.068206	0.121809
4	0.449508	0.270152	0.169874	0.074112	0.150692	0.085074	0.132709
6	0.449508	0.269731	0.169564	0.076822	0.153570	0.083003	0.132714
8	0.449508	0.269683	0.169068	0.079125	0.155540	0.083914	0.131502
10	0.449508	0.269748	0.169407	0.080213	0.157050	0.085329	0.131450

Table 5
Global approximation error ϵ_I (top panel) and ϵ_ϕ (bottom panel) as a function of N, L for the standard scattering map σ_1. The error is evaluated in the independent data set $I = 0.5, 1.5, 2.5, \dots, 6.5$. Compare to the original data set in Table 4.

	L							
N	0	1	2	3	4	5	6	7
2	0.680000	0.782085	0.367800	0.198887	0.233913	0.071975	0.104571	0.077636
4	0.680000	0.822172	0.465488	0.201108	0.227997	0.035848	0.062120	0.032394
6	0.680000	0.841491	0.497539	0.205914	0.224239	0.048805	0.052237	0.022763
8	0.680000	0.848342	0.499856	0.219921	0.216637	0.050972	0.053874	0.023362
10	0.680000	0.852520	0.491977	0.219181	0.209180	0.049182	0.054193	0.023105

	L						
N	0	1	2	3	4	5	6
2	0.370667	0.210922	0.112123	0.063086	0.107801	0.040273	0.067627
4	0.370667	0.213108	0.123612	0.057792	0.107593	0.040863	0.062113
6	0.370667	0.212718	0.122866	0.059556	0.109339	0.039459	0.062510
8	0.370667	0.212655	0.122537	0.059490	0.110579	0.039398	0.061885
10	0.370667	0.212716	0.122826	0.059643	0.111556	0.039633	0.061842

7. Inner map

Recall that the *inner flow* refers to the restriction of the RTBP flow to the normally hyperbolic invariant manifold Λ_c, while the *inner map* refers to the restriction of the first return map $\mathcal{F}$ to Λ_c^Σ. Abusing notation, the inner map will still be called $\mathcal{F}$.

As explained in Section 2.1, the RTBP flow on the center manifold $W^c(L_1)$ consists simply on a translation on the 2-torus,

$$\dot{J}_p = 0, \qquad \dot{\phi}_p = \frac{\partial H}{\partial J_p} =: \nu_p(J_p, J_v),$$
$$\dot{J}_v = 0, \qquad \dot{\phi}_v = \frac{\partial H}{\partial J_v} =: \nu_v(J_p, J_v).$$

The value of the planar and vertical frequencies ν_p, ν_v of the torus are obtained differentiating the Hamiltonian in Birkhoff normal form.

Upon restriction to the NHIM Λ_c, we get rid of the planar action J_p, which can be recovered if necessary using the energy condition, so the inner flow is

$$\dot{J}_v = 0, \quad \dot{\phi}_p = \nu_p(J_v), \quad \dot{\phi}_v = \nu_v(J_v). \tag{21}$$

Finally, the first return map of the inner flow to the section Σ is

$$J_v' = J_v, \quad \phi_v' = \phi_v + \frac{2\pi\nu_v(J_v)}{\nu_p(J_v)}.$$

In terms of the scaled coordinates I, ϕ, the inner map $\mathcal{F}: \Lambda_c^{N,\Sigma} \to \Lambda_c^{N,\Sigma}$ is given by

$$I' = I, \quad \phi' = \phi + \nu(I), \tag{22}$$

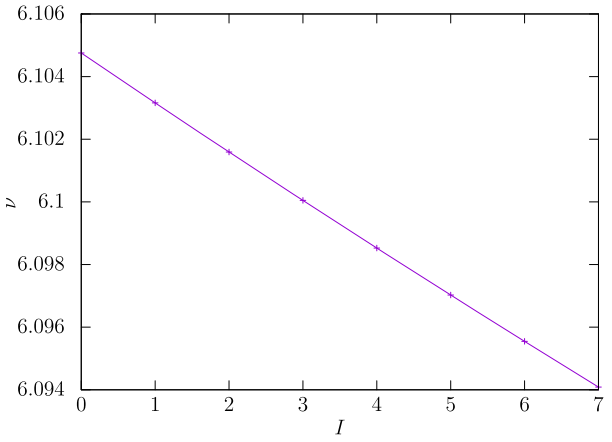

Fig. 13. The inner shift $\nu(I)$.

where we have introduced the new function

$$\nu(I) := \frac{2\pi\nu_v(I/1000)}{\nu_p(I/1000)}.$$

As seen in Fig. 13, the inner shift $\nu(I)$ decreases almost linearly with I. In particular, this shows that the inner map $\mathcal{F}$ is a twist map.

8. Phase space of the scattering map

In Sections 5 and 6, we have obtained a series representation of the scattering maps $\sigma(I,\phi)$ with small approximation error. This representation is valid on an annulus $\mathcal{A}$ inside the NHIM (see Eq. (20)). Thus we can now iterate the scattering map in $\mathcal{A}$.

To explore the global phase space of the scattering map, we perform the following experiment: Take 300×300 initial conditions evenly distributed in $\mathcal{A}$, and iterate each initial condition 100 times by the scattering map. The resulting phase space portrait is shown in Fig. 14.

Notice that the scattering map (13), rewritten as

$$\phi' = \phi - \omega(I) - \frac{\partial\widetilde{\mathcal{L}}}{\partial I}(I,\phi') \tag{23a}$$

$$I' = I + \frac{\partial\widetilde{\mathcal{L}}}{\partial\phi'}(I,\phi') \tag{23b}$$

can be seen as a perturbation of the integrable map $(I,\phi)\mapsto(I'=I,\phi'=\phi-\omega(I))$, as long as the derivatives of $\widetilde{\mathcal{L}}$ are small enough. The frequency $-\omega(I)$ represents the *phase shift* of the map $(I,\phi)\mapsto(I'=I,\phi'=\phi-\omega(I))$.

Since $\omega'(I)\neq 0$ (see Fig. 11), the integrable map $(I,\phi)\mapsto(I,\phi-\omega(I))$ is a twist map. Below we check that the scattering map is also a twist map. (See 'Twist Condition').

By KAM theory (for an area preserving map given by its generating function; see, for instance, Arnold and Avez [47], Haro [48]), when the derivatives of $\widetilde{\mathcal{L}}$ are small, we expect that many of the invariant tori of the integrable twist map persist.

8.1. Phase shift

The phase shift of the scattering map (23) is $\phi'-\phi=-\omega(I)-\frac{\partial\widetilde{\mathcal{L}}}{\partial I}(I,\phi')$. The divided differences of $\omega(I)$ are listed in Table 2. From these data we see that $|\tilde{c}_0|\gg|\tilde{c}_1|\gg|\tilde{c}_j|$ for $j=2,\dots,6$. Comparing with Table 1, we notice that $|\tilde{c}_0|\gg|\tilde{a}_j^n|,|\tilde{b}_j^n|$, $j=1,\dots,7$, $n=2,4,6,8$. This implies that $\frac{\partial\widetilde{\mathcal{L}}}{\partial I}$ is much smaller than $\omega(I)$, which is non-zero, at least for I small enough. This argument could be used to assert that the phase shift is non-zero in the local domain $\mathcal{A}_{\text{loc}}$.

To deal with the global domain $\mathcal{A}$, we determine the range of I values where the phase shift is non-zero. The phase shift is bounded by

$$-\omega(I)-\max_{\phi'}\left|\frac{\partial\widetilde{\mathcal{L}}}{\partial I}(I,\phi')\right|\le-\omega(I)-\frac{\partial\widetilde{\mathcal{L}}}{\partial I}(I,\phi')\le-\omega(I)+\max_{\phi'}\left|\frac{\partial\widetilde{\mathcal{L}}}{\partial I}(I,\phi')\right|.$$

We have computed these bounds explicitly, using the series expansions of $\omega(I)$ and $\frac{\partial\widetilde{\mathcal{L}}}{\partial I}(I,\phi')$. The result is shown in Fig. 15. Note that the phase shift for σ_1 is non-zero for all $I\in[1,7]$, while the phase shift for σ_2 (modulo π) is non-zero except possibly for a small range of I values close to $I=7$.

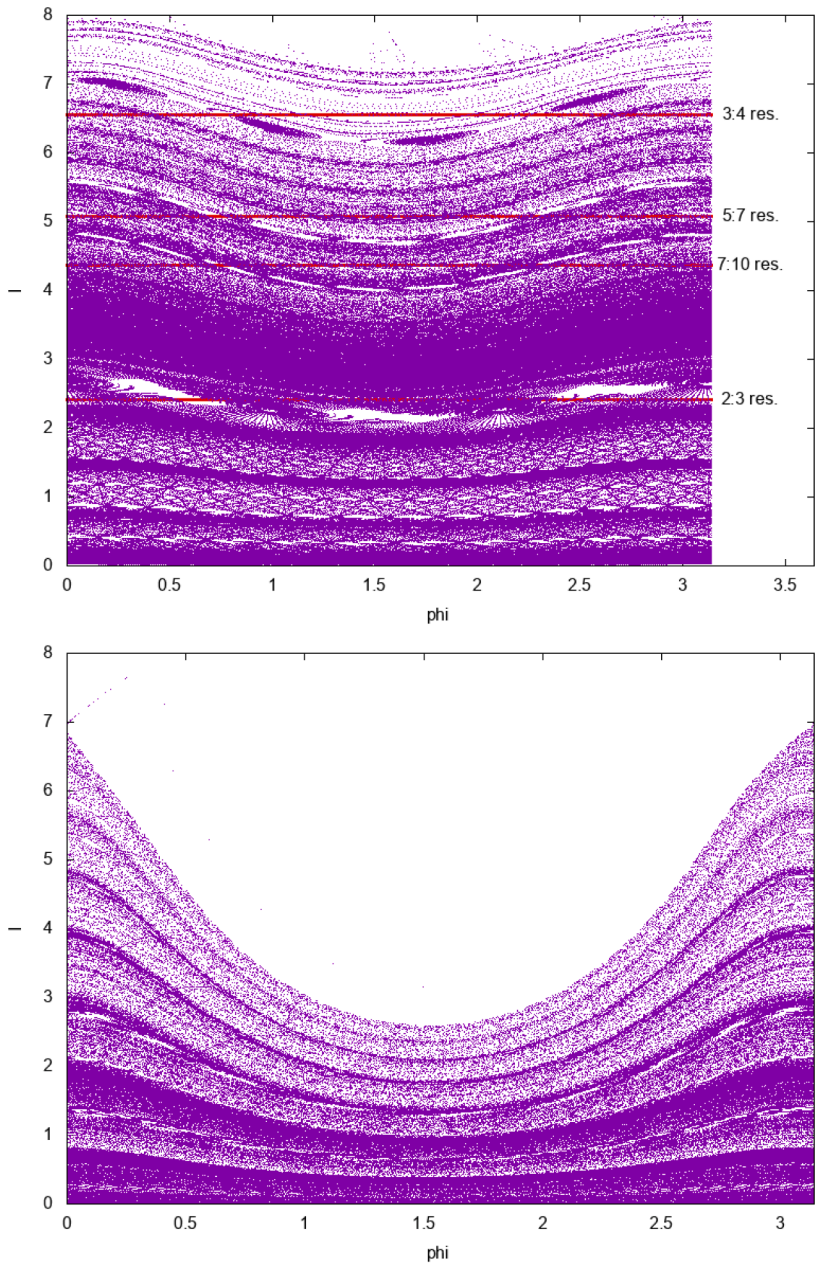

Fig. 14. Phase portrait of the scattering maps σ_1 (above) and σ_2 (below). The theoretical location of the main resonances, found in Section 9, is superimposed in red.

8.2. Twist condition

Let us compute the twist of the scattering map (23):

$$\frac{\partial \phi'}{\partial I}(I,\phi') = -\omega'(I) - \frac{\partial^2 \tilde{\mathcal{L}}}{\partial I^2}(I,\phi') - \frac{\partial^2 \tilde{\mathcal{L}}}{\partial \phi' \partial I}(I,\phi')\frac{\partial \phi'}{\partial I}.$$

Thus

$$\frac{\partial \phi'}{\partial I}(I,\phi') = -\frac{\omega'(I) + \frac{\partial^2 \tilde{\mathcal{L}}}{\partial I^2}}{1 + \frac{\partial^2 \tilde{\mathcal{L}}}{\partial \phi' \partial I}}, \tag{24}$$

provided that the denominator is non-zero.

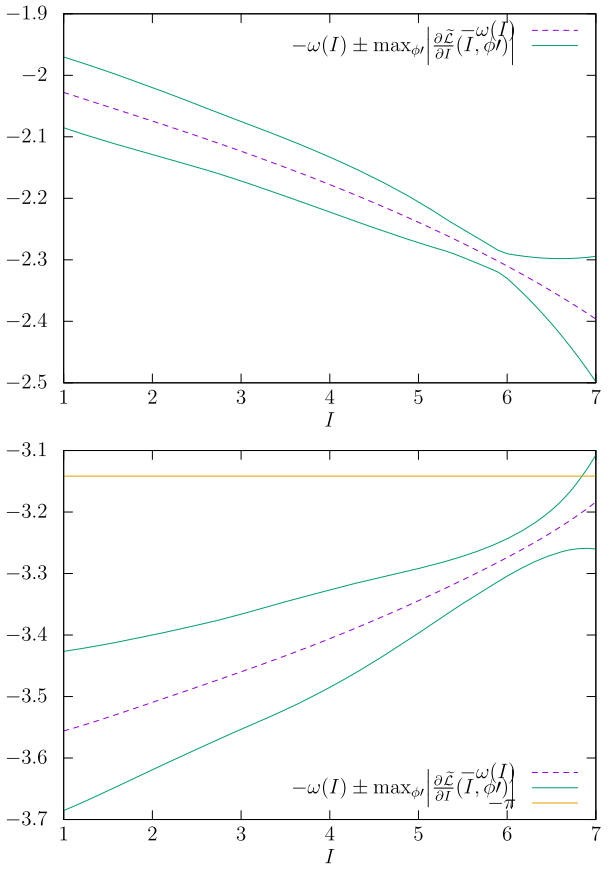

Fig. 15. Enclosure of the phase shift for the scattering map σ_1 (above) and σ_2 (below). The phase shift $-\omega(I) - \frac{\partial \widetilde{\mathcal{L}}}{\partial I}(I, \phi')$ is enclosed inside the green lines.

We have computed the twist (24) explicitly on the global domain $\mathcal{A}$, using the series expansions of $\omega(I)$ and $\widetilde{\mathcal{L}}(I, \phi')$. The result is shown in Fig. 16. Note that the twist for both σ_1 and σ_2 is non-zero in $\mathcal{A}$.

9. KAM tori and resonant zones for the scattering maps

As seen in Fig. 14, the phase portrait of the scattering maps σ_1, σ_2 is filled up with invariant curves and some resonant zones between them. Recall from Section 8 that both σ_1 and σ_2 are twist maps. To compute these invariant curves, we now introduce the exponential form in the sine-cosine Fourier expansion (16) of $\frac{\partial}{\partial \widetilde{\mathcal{L}}} \phi'$

$$\frac{\partial \widetilde{\mathcal{L}}}{\partial \phi'} = \sum_{n=1}^{N} A_n \cos n\phi' + \sum_{n=1}^{N} B_n \sin n\phi' = \sum_{n=-N, n\neq 0}^{N} C_n e^{in\phi'},$$

where $C = \left(C_{-n}, \dots, C_{-1}, C_1, \dots, C_N\right) \in \mathbb{C}^{2N}$ satisfies

$$C_n = \frac{1}{2}(A_n - iB_n), \quad C_{-n} = \frac{1}{2}(A_n + iB_n) = \overline{C_n}, \text{ for } n > 0.$$

Notice that for $\widetilde{\mathcal{L}} = 0$, or equivalently $C = 0$, any torus $I = I_0$ is invariant since then $I' = I_0$ in the expression (23b) of a scattering map, with an inner dynamics $\phi' = \phi - \omega_0$ given by (23a), where $\omega_0 := \omega(I_0)$.

For $\left|\widetilde{\mathcal{L}}\right|$ small enough, or equivalently $|C|$ small enough, a lot of these invariant curves survive. An invariant curve $I = I_0 + h(\phi)$ of a scattering map (23) satisfies $I' = I_0 + h(\phi')$, that is

$$h(\phi') = h\left(\phi' + \omega(I) + \frac{\partial \widetilde{\mathcal{L}}}{\partial I}(I, \phi')\right) + \frac{\partial \widetilde{\mathcal{L}}}{\partial \phi'}(I, \phi'), \text{ where } I = I_0 + h(\phi).$$

Expanding in C and h we get

$$h(\phi') = h(\phi' + \omega_0) + \frac{\partial \widetilde{\mathcal{L}}}{\partial \phi'}(I, \phi') + O(h\,C).$$

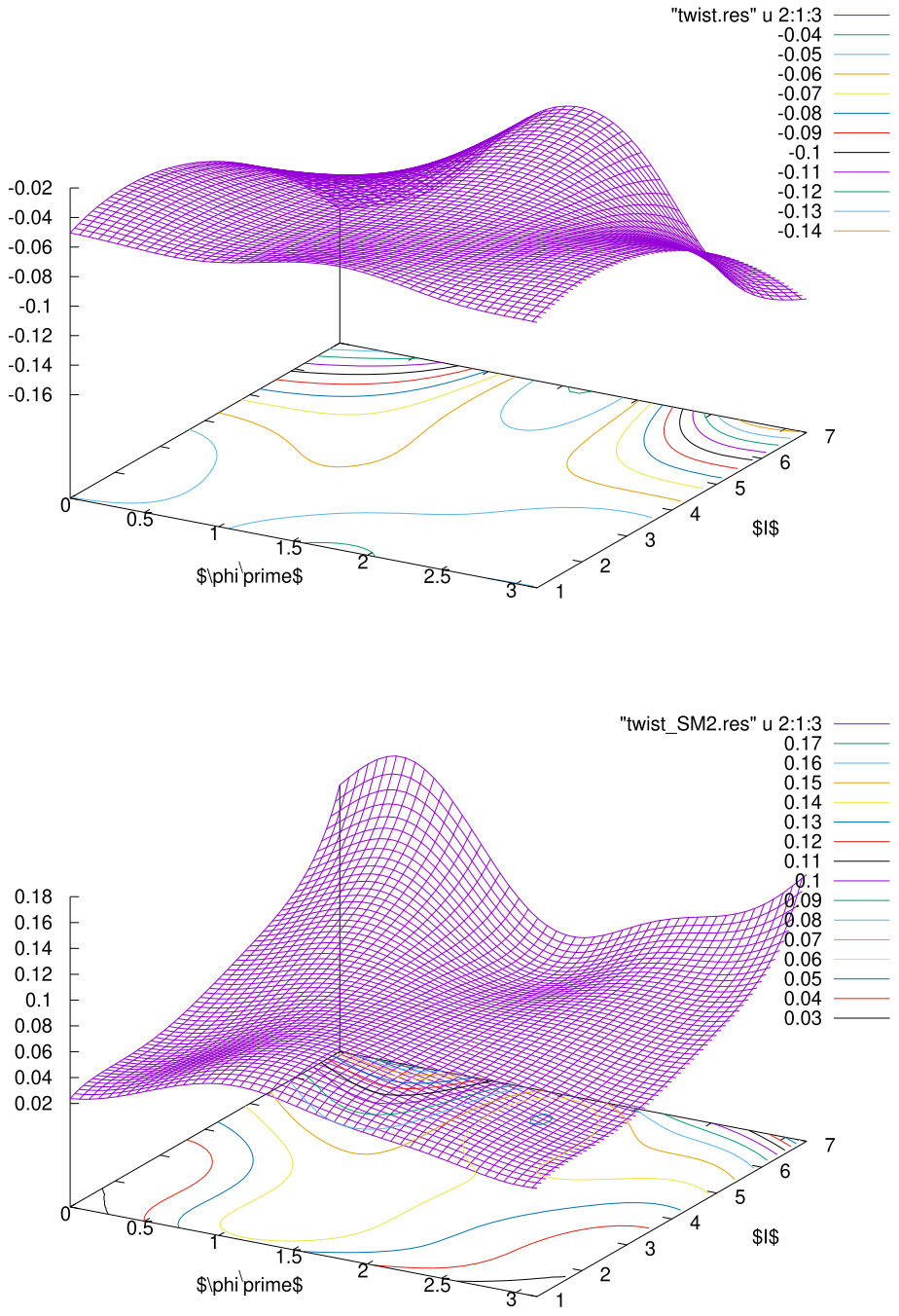

Fig. 16. Twist for the scattering map σ_1 (above) and σ_2 (below).

Writing $h(\phi') = \sum_{n=-N, n\neq 0}^{N} h_n e^{in\phi'}$ we get

$$\sum h_n e^{in\phi'} = \sum e^{in\omega_0} h_n e^{in\phi'} + \sum C_n e^{in\phi'} + O(hC),$$

which, equating Fourier coefficients, gives

$$h_n = -\frac{C_n}{e^{in\omega_0} - 1} + O(C^2) \text{ for } 0 < |n| \leq N.$$

For this approximate formula one needs that $\frac{n\omega_0}{2\pi} \notin \mathbb{Z}$ for $|n| \le N$ (non-resonant condition), and one sees that, up to order $O(C^2)$, the coefficients $h_n = O(C)$ are uniquely determined by C. KAM theorem consists in proving the convergence of these expansions for *diophantine frequencies* ω_0, using that σ_1 and σ_2 are twist maps.

9.1. Resonant zones for σ_1

Resonant zones for the symplectic map (13), or, equivalently, (23), where the KAM theorem does not provide invariant curves for small $\mathcal{L}$, appear around the values I such that $\frac{\omega(I)}{\pi}$ is a rational number. In the global setting,

$$\omega(I) = \Omega'(I) \approx \sum_{l=0}^{L} c_l N_l(I),$$

where the coefficients c_l are given in Table 2 for both scattering maps σ_1 and σ_2.

In particular for σ_1 (a totally analogous study for σ_2 can be carried out) $\frac{\omega(0)}{\pi} = 0.630128\ldots$, which is not too far for $2/3$ whose continued fraction is [1,2], which means that

$$\frac{2}{3} = [\mathbf{1}, \mathbf{2}] = \frac{1}{\mathbf{1} + \frac{1}{\mathbf{2}}}.$$

Therefore for I such that $\frac{\omega(I)}{\pi} = \frac{2}{3}$, which happens to be $I \approx 2.4175$, there should appear a resonance, indeed the largest one, since the width of the 'eyes' of a resonance is related to the denominator, in this case 3.

Other close rationals to 2/3 are given by close modified continued fractions. For instance

$$[\mathbf{1}, \mathbf{2}, \mathbf{1}] = \frac{1}{\mathbf{1} + \frac{1}{\mathbf{2} + \frac{1}{\mathbf{1}}}} = \frac{3}{4}.$$

We can compute some of the largest ones, ordered by their denominators:

I	$\frac{\omega(I)}{\pi}$	continued fraction
2.4175	$\frac{2}{3}$	[1,2]
6.5550	$\frac{3}{4}$	[1,2,1]
5.0752	$\frac{5}{7}$	[1,2,2]
4.3631	$\frac{7}{10}$	[1,2,3]
3.9523	$\frac{9}{13}$	[1,2,4]

The continued fraction of $\frac{2}{3}$ can be also written as [1,1,1], and smaller resonant values can be obtained for smaller continued fractions like $[1,1,1,3] = \frac{7}{11} = 0.636363\ldots$, etc

For the scattering map σ_1, the two main resonances are clearly visible near $I \approx 2.4175$ and $I \approx 6.5550$. See Fig. 14 (top panel).

10. Arnold diffusion

In this section we give details on the verification of the Numerical Result 1. Specifically, we verify numerically that the conditions of Theorem 1 are satisfied.

Let

$$\mathcal{A} = \{(I, \phi) \,|\, I \in [1, 7],\ \phi \in [0, 2\pi)\}$$

be the annulus where we want to show diffusion. The inner map f is $\mathcal{F}$ restricted to $\mathcal{A}$, and the system of scattering maps is either one of $\{\sigma_1\}$, $\{\sigma_2\}$, or $\{\sigma_1, \sigma_2\}$. Recall that f is a twist map. In Section 8 we verified numerically that σ_1 and σ_2 are twist maps as well.

As seen in Table 1, the harmonics of $\widetilde{\mathcal{L}}_i$ for both scattering maps σ_1 and σ_2, particularly those of degree two, are not zero, so that the inner map and any of these scattering maps can not have common invariant curves, and by Theorem 1 both the double dynamical systems $\{\mathcal{F}, \sigma_1\}$ and $\{\mathcal{F}, \sigma_2\}$ formed by the inner map and one of the scattering maps have diffusing pseudo-orbits along $\mathcal{A}$.

Even more, for the two scattering maps described in Table 1, one sees that the difference between the respective coefficients C_n is greater than 0.04 for the coefficients $C_{\pm 1}$ due to $\tilde{a}_1$. This, together with the fact that the magnitude of the denominator $e^{\pm i\omega_0} - 1$ in the formula of $h_{\pm 1}$ is much smaller than 1, prevents the two scattering maps from having common invariant curves, which, on the other hand, is clearly observed in the juxtaposition of the curves found numerically for the two scattering maps. This implies that the double dynamical system $\{\sigma_1, \sigma_2\}$ also has diffusing orbits along the NHIM.

We can take advantage of these dynamics to construct fast diffusing pseudo-orbits obtained from the triple dynamical system $\{\mathcal{F}, \sigma_1, \sigma_2\}$ formed by the inner map and the two scattering maps. We will give explicit constructions of diffusing pseudo-orbits, including fast ones, in Section 12.

Once such pseudo-orbits are obtained, the Shadowing Lemma Gidea et al. [44, Theorem 3.7] gives true orbits that shadow the pseudo-orbits, thus achieving Arnold diffusion.

Note that the above construction of diffusing pseudo-orbits assumes that the inner dynamics is derived from the Birkhoff normal form approximation, which is given by an integrable Hamiltonian. However, the original Hamiltonian is not integrable, and the NHIM Λ_c^Σ for the original Hamiltonian is not foliated by circles invariant under the true inner map. We will now argue the existence of diffusing orbits for the original system.

Recall that the inner map for the Birkhoff normal form is an integrable twist map, and the global error in the numerical integration of orbits with initial condition (J, ϕ_p, ϕ_v) is less than $10^{-12}/5000$; see Section 4. (We recall $J = J_v$ is the vertical amplitude of the motion.) Since each level set of J is preserved by the inner dynamics $\mathcal{F}$ for the Birkhoff normal form, and since $I = 1000J$, it follows that each essential invariant circle Γ for the inner map $\mathcal{F}$ for the original Hamiltonian is less than $\rho_1 = 10^{-12} < 10^{-9}/1500$ away from a level set of I.

We also know from Section 4.4 that the scattering maps σ_1, σ_2 are globally defined on $\mathcal{A}$. Moreover, for each I in the interval $[1, 7]$, the oscillation,

$$\sup_\phi \frac{\partial \widetilde{\mathcal{L}}_1}{\partial \phi'}(I, \phi') - \inf_\phi \frac{\partial \widetilde{\mathcal{L}}_1}{\partial \phi'}(I, \phi')$$

corresponding to σ_1, is bigger than $\rho_2 = 0.2$.

To see this, note that the smallest oscillations in Fig. 12(b) happen for the action level $I = 1$. Zooming in that action level (Fig. 17), it is clear that the oscillation is bigger than $\rho_2 = 0.2$. Alternatively, approximate the image of $I = 1$ by the truncated Fourier-Polynomial interpolation consisting of the dominant coefficients

$$I' = I + \tilde{a}_1^{(2)} \cos 2\phi' + \tilde{b}_1^{(2)} \sin 2\phi',$$

where $\tilde{a}_1^{(2)} = 0.178180$ and $\tilde{b}_1^{(2)} = -0.097275$ (See Table 1). This function has oscillations of size twice its amplitude $\sqrt{\left(\tilde{a}_1^{(2)}\right)^2 + \left(\tilde{b}_1^{(2)}\right)^2} = 0.203003$.

Similarly, the oscillation of $\frac{\partial \widetilde{\mathcal{L}}_2}{\partial \phi'}$ corresponding to σ_2 is bigger than 0.3.

These facts imply that no essential invariant circle Γ for $\mathcal{F}$ is invariant under σ_1 or σ_2. Therefore, Theorem 1 applies and there are orbits of the IFS $\{\mathcal{F}, \sigma_1\}$, as well as orbits of the IFS $\{\mathcal{F}, \sigma_2\}$, that go from the lower boundary of the annulus $\mathcal{A}$ to its upper boundary.

Again, the Shadowing Lemma Gidea et al. [44, Theorem 3.7] gives true orbits that shadow the obtained pseudo-orbits, thus achieving Arnold diffusion.

11. Time estimates for inner and transition map

One of our main goals is to estimate the drift time spent by drift orbits, constructed in Section 12. As an intermediate step, we measure the time spent on one iterate of the inner map ('inner time', or t_{in}), and the time spent on one iterate of the transition map ('outer time', or t_{out}).

In terms of the RTBP inner flow (21), one application of the inner map corresponds to integrating an initial condition $(J_v, \phi_p = 0, \phi_v) \in \Lambda_c^\Sigma$ during the amount of time that it takes to return to the section Σ. Thus, each iterate of the inner map takes time

$$t_{\text{in}} = \frac{2\pi}{\nu_p}.$$

Numerically, we find that $2.0764 < \nu_p(I) < 2.0781$, and therefore the inner time is bounded by

$$3.0235 < t_{\text{in}} < 3.0261.$$

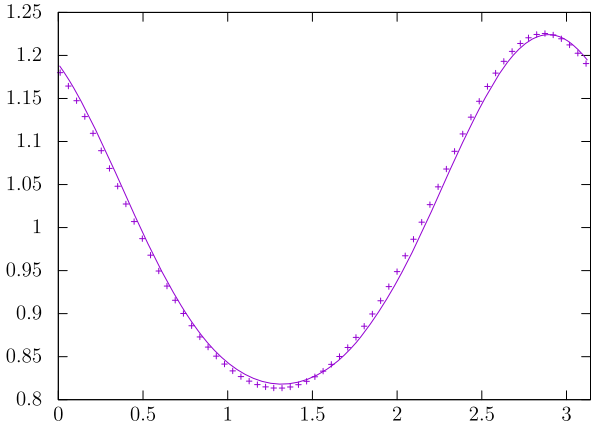

Fig. 17. Image of the action level $I = 1$ by the numerical scattering map (points) versus the scattering map series $N = 4, M = 5$ (lines).

In terms of the RTBP flow, one application of the transition map corresponds to a (segment of) a homoclinic trajectory from $y_- \in W^u_{\rm loc}(\Lambda_c)$ to $y_+ W^s_{\rm loc}(\Lambda_c)$. As noted in Section 4.2, the flight time of homoclinic segments is bounded by

$$5.936738 \le t_{\rm out} \le 6.000688.$$

Therefore in our setting we find that outer times $t_{\rm out}$ are approximately twice as long as inner times $t_{\rm in}$.

12. Drift orbits

In Section 10 we provided numerical evidence that the conditions of Theorem 1 are fulfilled, hence there exist trajectories that exhibit Arnold diffusion, characterized by a drift in the scaled vertical amplitude I (see (12)). Our arguments do not provide a way to find such orbits, much less those orbits that drift 'fast'.

In this section, we propose different algorithms to produce drift orbits, i.e., orbits of the iterated function system (IFS) consisting of the inner and outer map, whose action variable I increases from $I = 1$ to $I > 7$. We produce two different type of orbits:

- Orbits of the iterated function system $\{\mathcal{F}, \sigma_1\}$, $\{\mathcal{F}, \sigma_2\}$, or $\{\mathcal{F}, \sigma_1, \sigma_2\}$. These orbits are a realization of the existence Theorem 1. We look for short orbits, i.e. we try to minimize the number of iterates. However, it is important to realize that **these orbits do not directly translate to pseudo-orbits for the R3BP flow** (since one iterate of the scattering map does not correspond to a segment of homoclinic trajectory).
- Orbits of the iterated function system $\{\mathcal{F}, \tau_1\}$, $\{\mathcal{F}, \tau_2\}$, or $\{\mathcal{F}, \tau_1, \tau_2\}$. These are also a realization of the existence Theorem 1, and they **directly translate to pseudo-orbits of the R3BP flow**. Each iterate of the transition map corresponds to a segment of homoclinic trajectory. Using the time estimates of Section 11, we can estimate the total drift time of the pseudo-orbit as:

  $$t = n_0 t_{\rm in} + n_1 t_{\rm out} + n_2 t_{\rm out},$$

  where n_0, n_1 and n_2 denote the number of iterates of $\mathcal{F}$, τ_1 and τ_2 respectively. Keeping an eye on Astrodynamics applications, we want to minimize the total drift time.

12.1. *Double dynamical system* $\{\mathcal{F}, \sigma_i\}$. *Greedy algorithm*

In Section 9 we already established that σ_i $(i = 1, 2)$ has many invariant curves. All iterates of σ_i either belong to an invariant curve, or are confined between two invariant curves. Thus it is not possible to cross from $I = 1$ to $I > 7$ using just one scattering map σ_i.

However, according to Theorem 1, one can combine the inner and outer map to produce drift orbits. Now we will explicitly construct such drift orbits for the double dynamical system $\{\mathcal{F}, \sigma_i\}$.

Let us partition the domain $\mathcal{A}$ of the scattering map into three sets:

$$\mathcal{A} = \mathcal{A}_- \cup \mathcal{A}_0 \cup \mathcal{A}_+.$$

$\mathcal{A}_+$ denotes the subdomain where σ gains action, $\mathcal{A}_-$ where it looses action, and $\mathcal{A}_0$ where it neither gains nor looses action:

$$\mathcal{A}_+ = \{(I, \phi') \mid I' - I > 0\} = \left\{(I, \phi') \mid \frac{\partial \widetilde{\mathcal{L}}}{\partial \phi'}(I, \phi') > 0\right\}$$

$$\mathcal{A}_- = \{(I, \phi') \mid I' - I < 0\} = \left\{(I, \phi') \mid \frac{\partial \widetilde{\mathcal{L}}}{\partial \phi'}(I, \phi') < 0\right\}$$

$$\mathcal{A}_0 = \{(I, \phi') \mid I' - I = 0\} = \left\{(I, \phi') \mid \frac{\partial \widetilde{\mathcal{L}}}{\partial \phi'}(I, \phi') = 0\right\}.$$

These sets are readily identified in Fig. 18. For the first scattering map, $\mathcal{A}_0$ roughly consists of two vertical lines at $\phi' \approx 0.5$ and $\phi' \approx 2$, and $\mathcal{A}_+$ roughly consists of the vertical strip $(I, \phi') \in [1, 7] \times (2, 0.5)$. For the second scattering map, $\mathcal{A}_0$ roughly consists of two vertical lines at $\phi' \approx 1.25$ and $\phi' \approx 3$, and $\mathcal{A}_+$ roughly consists of the vertical strip $(I, \phi') \in [1, 7] \times (3, 1.25)$.

A simple strategy to produce drift orbits is to *always apply the scattering map if it increases the action* (even if the action gain $I' - I$ is small). Otherwise, apply the inner map.

This 'greedy' algorithm is guaranteed to produce a drift orbit independently of the initial condition, due to the following simple observations: In our model's domain $\mathcal{A}$ of validity,

- The inner map $(I', \phi') = \mathcal{F}(I, \phi)$, given in Eq. (22), is a twist map with frequency $\nu(I) \approx 6.1$ on the universal cover (see Fig. 13), or $\nu(I) \approx -0.2$ on the base space (where angles are identified modulo π). Thus the angle ϕ decreases approximately by 0.2 radians at every iterate of the inner map.
- Hence, for any given point $(I, \phi) \in \mathcal{A}$, its forward orbit by the inner map eventually enters $\mathcal{A}_+$.
- If (I, ϕ) already belongs to $\mathcal{A}_+$, we apply the scattering map, increasing the action. Else, we apply the inner map until the orbit enters $\mathcal{A}_+$, and then apply the scattering map.

For example, Fig. 19 shows the drift orbit produced starting from the initial condition $(I = 1, \phi = 0)$. Notice that the drift orbit produced by $\{\mathcal{F}, \sigma_1\}$ is much longer than the one produced by $\{\mathcal{F}, \sigma_2\}$. However, as explained before, these orbits do not directly translate to pseudo-orbits of the RTBP flow, and we don't have control over their drift time.

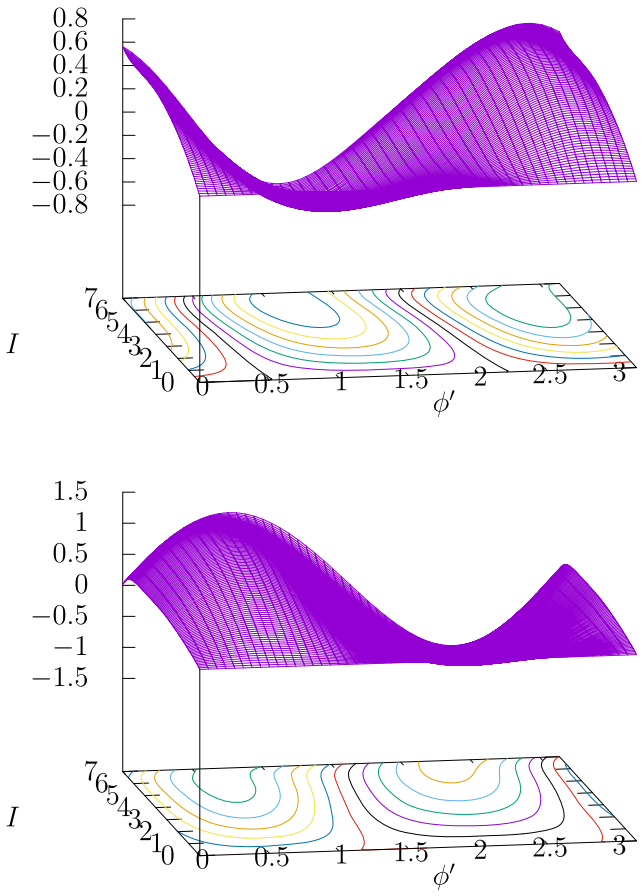

Fig. 18. The function $\frac{\partial \widetilde{\mathcal{L}}}{\partial \phi'}(I, \phi')$ for σ_1 (above) and σ_2 (below). Note that the function $\phi' \to \frac{\partial \widetilde{\mathcal{L}}}{\partial \phi'}(I_0, \phi')$ attains its maximum at $\phi' \approx 2.8$ (above) and $\phi' \approx 0.6$ (below).

12.2. Triple dynamical system $\{\mathcal{F}, \tau_1, \tau_2\}$. Shortest-time algorithm

The algorithms described in previous sections are relatively simple to implement, but they yield sub-optimal pseudo-orbits in terms of their drift time. Now we focus on finding the optimal drift time. This is specially challenging when combining three dynamical systems (inner map, transition map 1, and transition map 2) to construct the pseudo-orbit. Obviously we can't consider all the possible combinations of $\{\mathcal{F}, \tau_1, \tau_2\}$, since this number grows exponentially with respect to the length of the orbit. The main idea is to leverage the classic Dijkstra algorithm [49] for finding shortest paths in a graph.

First we partition the domain $\mathcal{A}$ into a uniform grid of $m \times n$ two-cells (rectangles) of equal size by dividing $I \in [1, 7]$ into m intervals and $\phi \in [0, \pi)$ into n intervals. (In practice, we will use $m = n = 30$, so the grid consists of 900 small cells).

We introduce a *directed* graph $G =< V, E >$ whose vertices V represent the different cells. An edge $e \in E$ from $u \in V$ to $v \in V$ means that the center point (I, ϕ) of cell u is mapped into cell v either by $\mathcal{F}$, τ_1, or τ_2. In each case, the edge records the 'distance' between cells, defined as the integration time corresponding to applying $\mathcal{F}$, τ_1, resp. τ_2.

More precisely, an edge from u to v is a pair $e = (map, distance)$, where

- $e = (\mathcal{F}, t_{\text{in}})$ if (I, ϕ) is mapped into v by the inner map;
- $e = (\tau_1, t_{\text{out}})$ if (I, ϕ) is mapped into v by the first transition map;
- $e = (\tau_2, t_{\text{out}})$ if (I, ϕ) is mapped into v by the second transition map;
- $e = (\emptyset, \infty)$ if (I, ϕ) is not mapped into v by neither map.

On rare occasions, τ_1 and/or τ_2 can map the center point (I, ϕ) to the same cell as the inner map. If this happens, the inner map is preferred since it takes shorter time, so we set the edge to $(\mathcal{F}, t_{\text{in}})$.

Remark 18. The image (I', ϕ') of (I, ϕ) by the transition map may be outside $\mathcal{A}$. However, this can only happen when $I' > 7$ (by construction, $I' < 0$ can never happen). In this case, we associate u with the closest cell v to the point (I', ϕ'), namely the cell containing $(7, \phi')$.

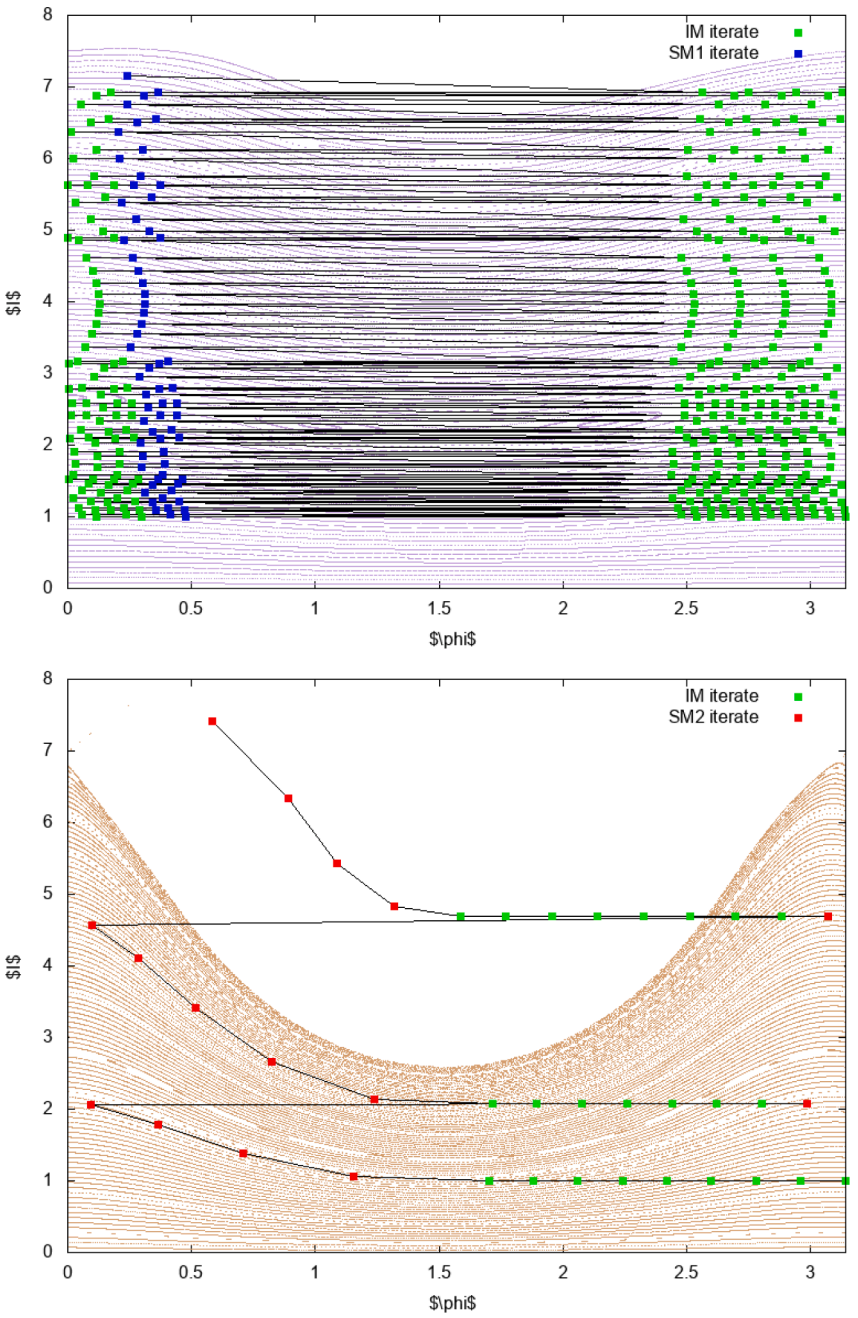

Fig. 19. Drift orbit of $\{\mathcal{F}, \sigma_1\}$ (top panel) and $\{\mathcal{F}, \sigma_2\}$ (bottom panel) using the greedy algorithm. Green points correspond to iterates of the inner map; blue (resp. red) points correspond to iterates of the first (resp. second) scattering map. Iterates have been joined by line segments to make the orbit more visible. For reference, the orbit is shown against a background consisting of the phase space of the scattering map.

Given a source cell s and a destination cell t, Dijkstra's algorithm applied to G provides the **shortest (directed) path in the graph** from s to t in terms of the distance defined above.

Notice that this path does not exactly correspond to an orbit of the IFS, since we have only considered iterates of center points to construct G (and the orbit does not necessarily pass through center points, but rather through arbitrary cell points). However, this path clearly *informs* the choice of map $\{\mathcal{F}, \tau_1, \tau_2\}$ that we should apply when the orbit passes through a given cell.

For example, suppose that the current iterate is inside cell u, and the shortest path from u to t starts with, say,

$$u \xrightarrow{(\tau_1, t_{\text{out}})} v \longrightarrow \ldots \longrightarrow t.$$

Then, the best choice given the available information is to apply the first transition map to the current iterate.

Our algorithm to construct optimal orbits (shortest drift time) is given in (Algorithm 1).

Algorithm 1 Shortest-time algorithm.

procedure ORBITSHORTESTTIME(x, y) ▷ Shortest-time orbit from point $x \in \mathcal{A}$ to (a neighborhood of) point $y \in \mathcal{A}$
  $t \leftarrow cell(y)$ ▷ Destination cell
  $orbit \leftarrow x$ ▷ Initialize orbit with x
  while $x \notin neighborhood(y)$ **do** ▷ End when close enough to y
    $u \leftarrow cell(x)$ ▷ Update current cell
    $path \leftarrow Dijkstra(u, t)$ ▷ Shortest path from u to t
    if $path$ starts with $\mathcal{F}$ **then**
      $x \leftarrow \mathcal{F}(x)$
    else if $path$ starts with τ_1 **then**
      $x \leftarrow \tau_1(x)$
    else ▷ $path$ starts with τ_2
      $x \leftarrow \tau_2(x)$
    end if
    $orbit \leftarrow concat(orbit, x)$ ▷ Add iterate x to orbit
  end while
  return $orbit$
end procedure

Fig. 20 shows the shortest-time orbit from $x = (I, \phi) = (1, 1.5)$ to a neighborhood of $y = (I, \phi) = (7, 1.5)$. The corresponding pseudo-orbit for the RTBP flow takes time $34t_{\text{in}} + 17t_{\text{out}} \approx 204$ RTBP time units, i.e. about 32 years (optimal drift time). Compare this to the orbits obtained in previous sections.

Notice that the optimal orbit uses all three dynamics ($\mathcal{F}$, τ_1 and τ_2) for maximum flexibility.

Notice that some iterates actually *decrease* the action. The key point is that, sometimes, one needs to take an iterate that decreases action in order to quickly move to a region where it later increases sharply. This way the pseudo-orbit's time is globally optimized.

Finally, from the orbit of the IFS $\{\mathcal{F}, \tau_1, \tau_2\}$ we can construct a pseudo-orbit by concatenating segments of trajectories of the RTBP flow. Each iterate of the inner map $\mathcal{F}$ corresponds to its flow suspension, which is integrated using the Birkhoff normal form. Each

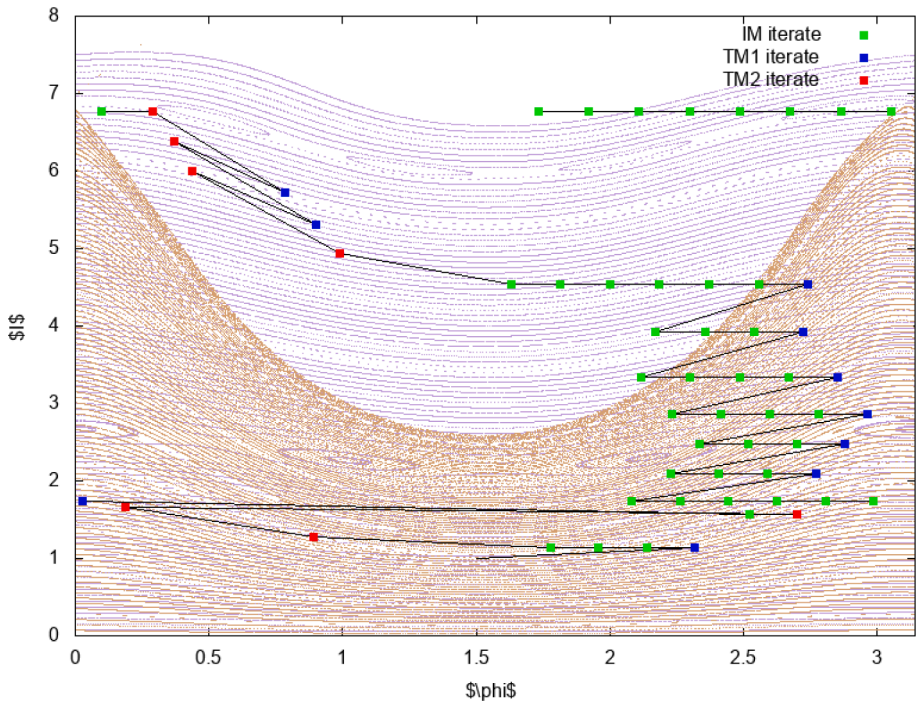

Fig. 20. Drift orbit of the triple system $\{\mathcal{F}, \tau_1, \tau_2\}$ using the shortest path algorithm. Notice that some iterates of the transition map actually *reduce* the action, in order to increase it more efficiently overall.

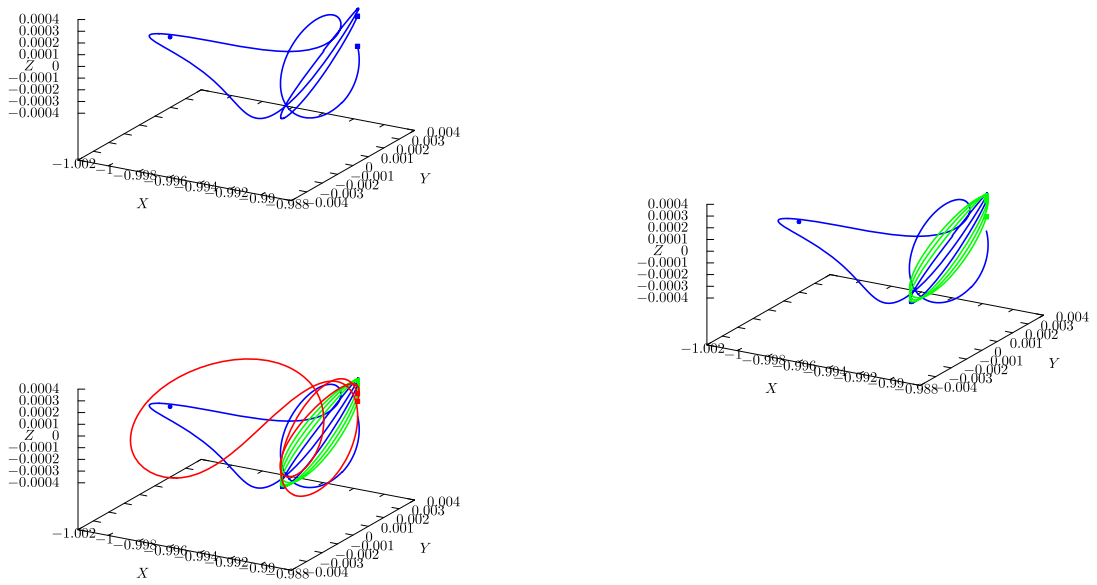

Fig. 21. Top left: Trajectory segment corresponding to the first application of τ_1 in Fig. 20 (endpoints are marked with squares). The Earth is represented by a blue circle (not to scale). Middle right: Segments corresponding to $\tau_1 \circ \mathcal{F}^3$. Bottom left: Segments corresponding to $\tau_1 \circ \mathcal{F}^3 \circ \tau_2$.

iterate of the transition map τ_1 or τ_2 corresponds to a finite piece of homoclinic trajectory, which is computed by continuation of those previously found in Section 4.

Fig. 21 illustrates the construction of the pseudo-orbit corresponding to the orbit in Fig. 20: First, τ_1 is applied once; this corresponds to the blue homoclinic segment. Then $\mathcal{F}$ is applied three times; this corresponds to the green segment. Next, τ_2 is applied once; this corresponds to the homoclinic red segment. Notice that all segments start and end on the Poincaré section Σ (endpoints are marked with squares). This construction would continue until the whole pseudo-orbit is obtained (not displayed).

Remark 19. We have obtained a pseudo-orbit, not a true trajectory of the RTBP. The endpoints of consecutive segments do not exactly match in positions or velocities, but the discontinuities are small (as is apparent in Fig. 21). In fact, the velocity discontinuities $\Delta v = \|(\Delta\dot{X}, \Delta\dot{Y}, \Delta\dot{Z})\|$, are smaller than 3.5×10^{-4}. Since the complete pseudo-orbit consists of 27 consecutive segments, the total required thrust is less than $26 \times 3.5 \times 10^{-4} \approx 0.0091$ non-dimensional RTBP units. When converted into metric units, this amounts to 271 m/s.

Of course, to this pseudo-orbit one can apply shadowing results Gidea et al. [44, Theorem 3.7] to establish the existence of a true RTBP trajectory that shadows it. For applications, however, obtaining the pseudo-orbit is often the crucial step, since it is ultimately refined in a much more realistic model than the RTBP, e.g. using JPL's Ephemeris.

CRediT authorship contribution statement

Amadeu Delshams: Validation, Writing – original draft, Conceptualization, Writing – review & editing, Methodology; **Marian Gidea:** Writing – original draft, Conceptualization, Writing – review & editing, Methodology, Validation; **Pablo Roldan:** Writing – original draft, Methodology, Writing – review & editing, Software, Validation, Conceptualization.

Data availability

Data will be made available on request.

Declaration of competing interest

The authors declare that they have no known competing financial interests or personal relationships that could have appeared to influence the work reported in this paper.

Acknowledgement

AD and PR supported by Spanish grant PID2021-123968NB-I00 (MI-CIU/AEI/10.13039/501100011033/FEDER/UE). Research of M.G. was partially supported by NSF grant DMS-2307718 and DMS-2154725. The authors are very grateful to the anonymous reviewers for their comments and suggestions that have contributed to improving this article in a very significant way.

References

[1] Delshams A, de la Llave R, Seara TM. A geometric approach to the existence of orbits with unbounded energy in generic periodic perturbations by a potential of generic geodesic flows of $\mathbf{T}^2$. Commun Math Phys 2000;209(2):353–92. https://doi.org/10.1007/PL00020961.
[2] Delshams A, de la Llave R, Seara TM. A geometric mechanism for diffusion in Hamiltonian systems overcoming the large gap problem: heuristics and rigorous verification on a model. Mem Am Math Soc 2006;179(844):viii + 141. https://doi.org/10.1090/memo/0844.
[3] Delshams A, de la Llave R, Seara TM. Orbits of unbounded energy in quasi-periodic perturbations of geodesic flows. Adv Math 2006;202(1):64–188. https://doi.org/10.1016/j.aim.2005.03.005.
[4] Delshams A, de la Llave R, Seara TM. Geometric properties of the scattering map of a normally hyperbolic invariant manifold. Adv Math 2008;217(3):1096–153. https://doi.org/10.1016/j.aim.2007.08.014.
[5] Delshams A, Gidea M, Roldán P. Transition map and shadowing lemma for normally hyperbolic invariant manifolds. Discrete Contin Dyn Syst 2013;33(3):1089–112. https://doi.org/10.3934/dcds.2013.33.1089.
[6] Canalias E, Delshams A, Masdemont JJ, Roldán P. The scattering map in the planar restricted three body problem. Celest Mech Dyn Astron 2006;95(1–4):155–71. https://doi.org/10.1007/s10569-006-9010-4.
[7] Delshams A, Gidea M, Roldan P. Arnold's mechanism of diffusion in the spatial circular restricted three-body problem: a semi-analytical argument. Phys D 2016;334:29–48. https://doi.org/10.1016/j.physd.2016.06.005.
[8] Delshams A, Schaefer RG. Arnold diffusion for a complete family of perturbations. Regul Chaotic Dyn 2017;22(1):78–108. https://doi.org/10.1134/S1560354717010051.
[9] Delshams A, Schaefer RG. Arnold diffusion for a complete family of perturbations with two independent harmonics. Discrete Contin Dyn Syst 2018;38(12):6047–72. https://doi.org/10.3934/dcds.2018261.
[10] Delshams A, Masdemont J, Roldán P. Computing the scattering map in the spatial Hill's problem. Discrete Contin Dyn Syst Ser B 2008;10(2–3):455–83. https://doi.org/10.3934/dcdsb.2008.10.455.
[11] Arnold VI. Instability of dynamical systems with several degrees of freedom. Sov Math Dokl 1964;5:581–5. See also *Vladimir I. Arnold—collected works. Vol. I*, Springer-Verlag, Berlin, 2009, pp. 423–427, https://doi.org/10.1007/978-3-642-01742-1, or *Hamiltonian Dynamical Systems*, edited by R.S MacKay, J.D Meiss, CRC Press, 2020, pp. 633–637, https://doi.org/10.1201/9781003069515.
[12] Chierchia L, Gallavotti G. Drift and diffusion in phase space. Ann Inst H Poincaré Phys Théor 1994;60(1):144.
[13] Bolotin S, Treschev D. Unbounded growth of energy in nonautonomous Hamiltonian systems. Nonlinearity 1999;12(2):365.
[14] Treschev D. Evolution of slow variables in near-integrable Hamiltonian systems. In: Progress in nonlinear science, vol. 1 (Nizhny Novgorod, 2001). RAS, Inst. Appl. Phys., Nizhny Novgorod; 2002, p. 166–9.
[15] Mather JN. Arnol'd diffusion. I. Announcement of results. J Math Sci (N Y) 2004;124(5):5275–89.
[16] Treschev D. Evolution of slow variables in a priori unstable Hamiltonian systems. Nonlinearity 2004;17(5):1803–41.
[17] Piftankin GN. Diffusion speed in the Mather problem. Dokl Akad Nauk 2006;408(6):736–7.
[18] Gelfreich V, Turaev D. Unbounded energy growth in Hamiltonian systems with a slowly varying parameter. Commun Math Phys 2008;283(3):769–94. https://doi.org/10.1007/s00220-008-0518-1.
[19] Delshams A, Huguet G. Geography of resonances and Arnold diffusion in a priori unstable Hamiltonian systems. Nonlinearity 2009;22(8):1997–2077. https://doi.org/10.1088/0951-7715/22/8/013.
[20] Cheng C-Q, Yan J. Arnold diffusion in Hamiltonian systems: a priori unstable case. J Differ Geom 2009;82(2):229–77. http://projecteuclid.org/euclid.jdg/1246888485.
[21] Mather JN. Arnold diffusion by variational methods. In: Essays in mathematics and its applications. Springer, Heidelberg; 2012, p. 271–85. https://doi.org/10.1007/978-3-642-28821-0_11.
[22] Kaloshin V, Zhang K. Arnold diffusion for smooth convex systems of two and a half degrees of freedom. Nonlinearity 2015;28(8):2699–720. https://doi.org/10.1088/0951-7715/28/8/2699
[23] Bernard P, Kaloshin V, Zhang K. Arnold diffusion in arbitrary degrees of freedom and normally hyperbolic invariant cylinders. Acta Math 2016;217(1):1–79.
[24] Cheng C-Q, Xue J. Variational approach to Arnold diffusion. Sci China Math 2019;62(11):2103–30.
[25] Treschev D. Arnold diffusion far from strong resonances in multidimensional *a priori* unstable Hamiltonian systems. Nonlinearity 2012;25(9):2717–57. https://doi.org/10.1088/0951-7715/25/9/2717.
[26] Gidea M, de la Llave R. Perturbations of geodesic flows by recurrent dynamics. J Eur Math Soc (JEMS) 2017;19(3):905–56. https://doi.org/10.4171/JEMS/683.
[27] Gelfreich V, Turaev D. Arnold diffusion in a priori chaotic symplectic maps. Commun Math Phys 2017;353(2):507–47. https://doi.org/10.1007/s00220-017-2867-0.
[28] Gidea M, Marco J-P. Diffusing orbits along chains of cylinders. Discrete Contin Dyn Syst 2022;42(12):5737–82. https://doi.org/10.3934/dcds.2022121.
[29] Kaloshin V, Zhang K. Arnold diffusion for smooth systems of two and a half degrees of freedom; vol. 208 of *Annals of mathematics studies*. Princeton University Press, Princeton, NJ; 2020. ISBN 978-0-691-20253-2; 978-0-691-20252-5; 978-0-691-20493-2.
[30] Delshams A, Kaloshin V, de la Rosa A, Seara TM. Global instability in the restricted planar elliptic three body problem. Commun Math Phys 2019;366(3):1173–228. https://doi.org/10.1007/s00220-018-3248-z.
[31] Guardia M, Paradela J, Seara TM. A degenerate Arnold diffusion mechanism in the restricted 3 body problem. arXiv:230206973 2023.
[32] Clarke A, Fejoz J, Guardia M. Why are inner planets not inclined? Publ Math l'IHÉS 2024; https://doi.org/10.1007/s10240-024-00151-z.
[33] Capiński MJ, Gidea M, de la Llave R. Arnold diffusion in the planar elliptic restricted three-body problem: mechanism and numerical verification. Nonlinearity 2017;30(1):329–60. https://doi.org/10.1088/1361-6544/30/1/329.
[34] Capiński MJ, Gidea M. Arnold diffusion, quantitative estimates, and stochastic behavior in the three-body problem. Commun Pure Appl Math 2023;76(3):616–81. https://doi.org/10.1002/cpa.22014.
[35] Figueras J-L, Haro A. Sun–Jupiter–Saturn system may exist: a verified computation of quasiperiodic solutions for the planar three-body problem. J Nonlinear Sci 2025;35(1):13. https://doi.org/10.1007/s00332-024-10109-4.
[36] Belbruno E Capture dynamics and chaotic motions in celestial mechanics: with applications to the construction of low energy transfers. Princeton University Press; 2004.
[37] Gómez G, Koon WS, Lo MW, Marsden JE, Masdemont J, Ross S. Invariant manifolds, the spatial three-body problem and space mission design. Adv Astron Sci 2001;109, AAS paper 01–301:3–22. https://www.cds.caltech.edu/~marsden/bib/2001/14-GoKoLoMaMaRo2001/GoKoLoMaMaRo2001.pdf.
[38] Barcelona M, Haro A, Mondelo J-M. Semianalytical computation of heteroclinic connections between center manifolds with the parameterization method. SIAM J Appl Dyn Syst 2024;23(1):98–126. https://doi.org/10.1137/23M1547883.
[39] Jorba A, Masdemont J. Dynamics in the center manifold of the collinear points of the restricted three body problem. Phys D 1999;132(1–2):189–213. https://doi.org/10.1016/S0167-2789(99)00042-1.
[40] Jorba A. A methodology for the numerical computation of normal forms, centre manifolds and first integrals of Hamiltonian systems. Exp Math 1999;8(2):155–95. http://projecteuclid.org/euclid.em/1047477059.
[41] Capiński MJ, Roldán P. Existence of a center manifold in a practical domain around L_1 in the restricted three-body problem. SIAM J Appl Dyn Syst 2012;11(1):285–318. https://doi.org/10.1137/100810381.
[42] Moeckel R. Generic drift on cantor sets of annuli. In: Celestial mechanics (Evanston, IL, 1999); vol. 292 of *Contemp. Math.* Amer. Math. Soc., Providence, RI. ISBN 0-8218-2902-5; 2002, p. 163–71. https://doi.org/10.1090/conm/292/04922.
[43] Le Calvez P. Drift orbits for families of twist maps of the annulus. Ergodic Theory Dyn Syst 2007;27(3):869–79.
[44] Gidea M, de la Llave R, M-Seara T. A general mechanism of diffusion in Hamiltonian systems: qualitative results. Commun Pure Appl Math 2020;73(1):150–209. https://doi.org/10.1002/cpa.21856.

[45] Delshams A, Gutiérrez P. Estimates on invariant tori near an elliptic equilibrium point of a Hamiltonian system. J Differ Equ 1996;131(2):277–303. https://doi.org/10.1006/jdeq.1996.0165.
[46] Milnor J. Morse theory; vol. No. 51 of *Annals of mathematics studies*. Princeton University Press, Princeton, NJ; 1963. Based on lecture notes by M. Spivak and R. Wells.
[47] Arnold VI, Avez A. Ergodic problems of classical mechanics. W. A. Benjamin, Inc., New York-Amsterdam; 1968. Translated from the French by A. Avez.
[48] Haro A. An algorithm to generate canonical transformations: application to normal forms. Phys D 2002;167(3–4):197–217. https://doi.org/10.1016/S0167-2789(02)00459-1.
[49] Dijkstra EW. A note on two problems in connexion with graphs. Numer Math 1959;1:269–71. https://doi.org/10.1007/BF01386390.